12-15-2010

Modeling of Aortic Valve Anatomic Geometry from Clinical Multi Detector-Row Computed Tomography Images

Gregory A. Book
gbook@gbook.org

Modeling of Aortic Valve Anatomic Geometry from Clinical Multi Detector-Row Computed Tomography Images

Gregory Alexander Book

B.S., University of Connecticut, 2002

A Thesis

Submitted in Partial Fulfillment of the

Requirements for the Degree of

Master of Science

at the

University of Connecticut

2010

Approval Page

Master of Science Thesis

Modeling of Aortic Valve Anatomic Geometry from Clinical Multi Detector-Row Computed Tomography Images

Presented by

Gregory Alexander Book

Major Advisor _____

Wei Sun, PhD

Associate Advisor _____

Quing Zhu, PhD

Associate Advisor _____

Charles Primiano, MD

University of Connecticut

2010

Acknowledgements

I would like to thank my advisor, Prof Wei Sun, for helping me through my graduate education and pushing me to become a better researcher. His insistence on doing the best work I can showed me that good research does not come by chance, instead it comes about from hard work and persistence. I would also like to thank the entire Tissue Mechanics Laboratory at the University of Connecticut for their interest in imaging of the aortic valve, which allowed me to pursue a fascinating thesis topic. Particularly I would like to thank Qian Wang for his assistance creating 3D models of the aortic valve from which much of the 3D measurement and HDW work in this thesis is based, and Sonia Ortiz for her assistance with 2D image analysis and point distribution model creation.

I would also like to thank the PACS team and the staff of the cardiac catheterization lab at Hartford Hospital for assisting me with data collection. In particular the PACS team showed me how to get hundreds of medical imaging studies from a system which is only designed to retrieve a few at a time. The faculty of the Olin Neuropsychiatry Research Center allowed me to use their computer systems to retrieve the imaging data, but also allowed me to continue working there while I pursued my graduate education.

Most importantly, I thank my wife Lisa, daughter Rachel, and my entire family for their support while I was in school. I simply would not have been able to pursue a graduate degree without their help. I also thank my sister, Wendy Book MD of Emory University, for her availability to answer questions on topics of cardiology with which I was totally unfamiliar.

Research for this project was funded in part by Connecticut Department of Public Health Biomedical Research Grant DPH2010-0085 and AHA SDG No. 0930319N.

Table of Contents

Abstract

Transcatheter aortic valve implantation (TAVI) is an emerging and viable alternative to surgical valve replacement. A TAVI procedure involves insertion of a catheter into the heart through an artery or transapically, and expanding valve stent in place. This procedure dramatically reduces the recovery time by eliminating the need for open heart surgery. Understanding the biomechanics of the stent-valve interaction is crucial for proper device deployment and function. In this study, we examine the extraction of valve geometries and creation of valve models from multi-detector row computed tomography (MDCT) images that may eventually be used to model stent expansion on a patient specific basis.

Our study accomplished three specific goals using clinical 64-slice CT data from Hartford Hospital. First, manual measurement of a variety of aortic root anatomic dimensions was performed on 95 patients using standard methods, to which other measurement methods could be compared. Second, we investigated automatic 2D measurement and a 3D measurement technique and compared them to the standard measurements. Both 2D automatic and 3D manual measurements were similar to the standard manual measurements, but 3D providing more insight into valve shape for TAVI sizing and positioning. Third, we investigated the use of statistical shape models (SSMs) to perform automatic 3D model creation. Training of 3D SSMs is extremely labor-intensive and prone to error because of the manual landmarking step, so we created a novel method to perform automatic landmarking of training data. Our method used high dimensional warping (HDW) to propagate landmarks from a template model. We used this landmarking method to create point distribution models of the aortic valve from patient data. Future work would include completion of the 3D SSM implementation using active appearance models.

1- Introduction/Background

1.1 - The Heart and the Aortic Valve

The human heart consists of four chambers and four valves and is analogous to a pump which circulates blood. Starting at the left ventricle, which is largest chamber of the heart, oxygenated blood is pumped through the aortic valve into the aorta which supplies oxygenated blood to the organ systems of the body. Deoxygenated blood is returned through veins, is emptied into the right atrium, and is then pumped through the tricuspid valve into the right ventricle and then through the pulmonary valve into the pulmonary circuit. Once blood is in the pulmonary circuit, it becomes oxygenated as it passes the alveoli of the lungs and returns to the left atrium. Oxygenated blood from the left atrium is pumped through the mitral valve into the left ventricle to complete the circuit (figure 1) [1].

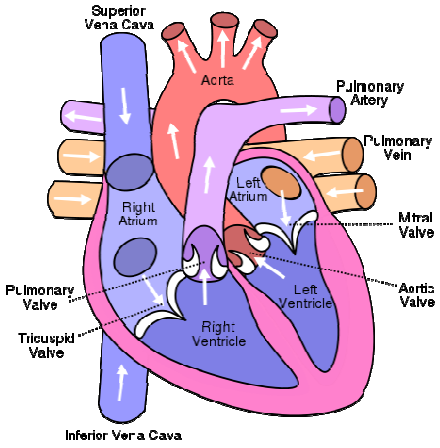

Figure 1 - Human heart with blood flow directions (source: Wikimedia Commons)

A heart beat occurs when the heart muscle contracts in a single rhythmic motion, starting at the atria and finishing with the contraction and relaxation of the ventricles. This motion occurs during the first 40% of the cardiac cycle with the heart at rest during the remaining time (figure 2). Systole describes the phase of the cardiac cycle when the heart is in contraction, and diastole the phase when the heart is at rest. An electrocardiogram (ECG) tracing is shown in figure 2. Significant events indicated by changes in electrical waveform

correspond to muscle contractions and are labeled P-Q-R-S-T. Point P corresponds to the atria contracting and points QRS correspond to the ventricles contracting, with ventricle relaxation and repolarization at point T. A full cycle of the heart rhythm is considered to occur between subsequent R peaks, called the R-R interval. Dividing the space in the R-R interval into 10% increments, the heart cycle can be viewed at specific time points, which is useful for gating multi detector-row computed tomography (MDCT) scan collection. MDCT images collected at 70% phase are ideal for analysis because the heart is in diastole and motion is at its minimum, producing clearer images (figure 2).

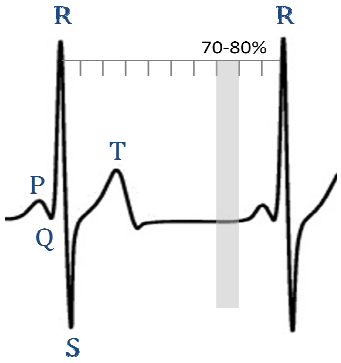

Figure 2 - ECG trace of a complete cardiac cycle, separated into 10% phase increments

All four heart valves open and close during each heart beat, approximately 103,000 times per day, however the aortic valve experiences the highest pressures of the four valves [2]. Because the aortic valve is subjected to the highest pressure of the circulatory system, it is often the first valve to deteriorate and develop disease with age.

The aortic valve is a tri-leaflet semi-lunar valve which controls outflow of blood from the left ventricle before it enters the systemic circulatory system. Blood leaves the left ventricle and passes through the aortic valve during systole, but is prevented from returning to the ventricle when the value closes during diastole.

Despite being a simple structure, descriptions of aortic anatomy are not consistent in the literature [3, 4]. To ensure consistent measurements within this study, we define our anatomical descriptions and provide justification for those definitions. We combined the most common anatomic descriptions with measurements that made the most sense for aortic valve assessment from MDCT images. Beginning at the base of the aortic valve (figure 3, 4a), inside the left ventricle, we describe the annulus ring as the perimeter of the aortic root below the leaflet attachment points. This perimeter was chosen because it is slightly away from the leaflet attachment points and thus the perimeter is contiguous and uninterrupted by the leaflets. Histologically, the aortic annulus is the junction between the aorta and the left ventricle.

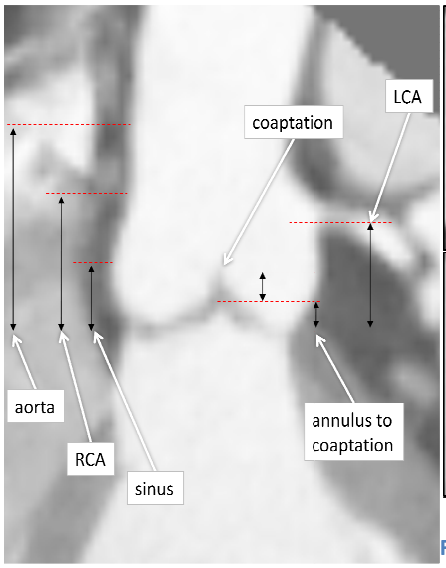

Figure 3 - Long axis view of the aortic root with distance-to-annulus measurements in a MDCT image

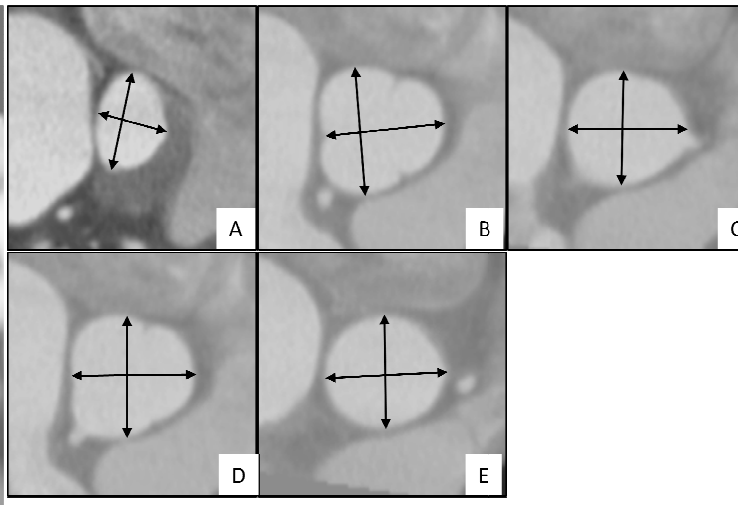

Figure 4 - Short axis views of the aortic root with manual measurement lines marked. Obtained from MDCT images. A) annulus B) sinus of Valsalva C) aortic root at left coronary ostium D) aortic root at right coronary ostium E) ascending aorta

Aortic valve leaflets attach just above the annulus ring, with each leaflet occupying a nearly equal length attachment site in the valve body. As shown in figure 3, the leaflets attachment site is higher than the lowest portion of the belly of the leaflets. The sinus of Valsalva is a barrel shaped cavity which contains the leaflets, leaflet attachment sites, and

coronary ostia (figure 3). The left and right coronary arteries, which supply oxygenated blood to the heart muscles, attach to the sinus of Valsalva above the leaflet coaptation at locations called the coronary ostia (figures 3 & 4c,d). Leaflet coaptation was defined as the central length along which all three leaflets touch, and this length is within the sinus of Valsalva (figure 3).

The sinotubular junction (STJ) is defined as the transition between the aortic valve and the ascending aorta, but in practice the STJ appears as a gradual transition between the SOV and the aorta and always occurs above the coronary ostia (figure 3). Distal to the annulus is the aorta (figure 3,4e). Because of the location of the aortic valve at the beginning of the aorta, the valve is often referred to as the aortic root.

Assuming no congenital defects, and no early age diseases such as rheumatoid arthritis, the aortic valve should function normally through most of a patient's life. Valve leaflets tend to thicken with age, especially at the leaflet free edge (figure 6), however this process is not enough to significantly reduce cardiac function [5]. In patients with hypertension, the leaflets of the valve can become hardened in a process called sclerosis, eventually developing calcified nodules which grow and cause a narrowing of the valve opening, causing stenosis.

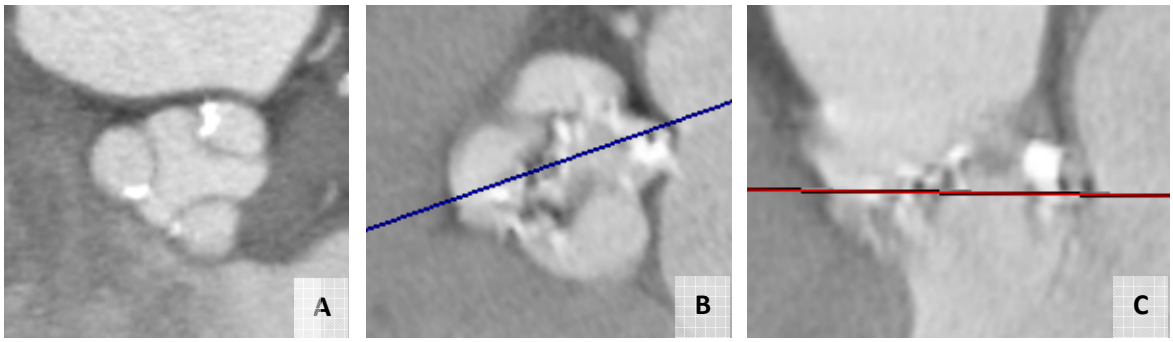

Figure 5 - Resliced images of calcification (bright spots) from MDCT studies. A) short axis view of moderate calcification B) short axis view of severe calcification and stenosis C) long axis view of severe calcification

Aortic stenosis is a common valvular disease in the United States and Europe characterized by thickening of the valve leaflets, decreased pliability and mobility, calcification of the aortic valve, and either decreased valve orifice size (stenosis) or leaking (regurgitation). Aortic valve leaflets close tightly in healthy patients, but as the leaflets harden and calcify they cannot completely close and a gap develops between leaflets (figure 5b,c). The gap allows blood to flow back into the left ventricle during diastole, causing aortic regurgitation. An alternate problem occurs when the leaflets fuse and cause a narrowing of the valve orifice. Prolonged regurgitation or stenosis will cause the body to compensate by forcing the left ventricle to work harder to pump blood and eventually cause left ventricular hypertrophy. Ventricular hypertrophy is a normal body response to decreased cardiac output, however the function of the heart will decline as long as the gap in the valve exists. If untreated, the patient will eventually develop congestive heart failure. Aortic stenosis is quite prevalent in the population: a 1983 study of found aortic stenosis in 44% of patients during autopsy following death by natural causes [6].

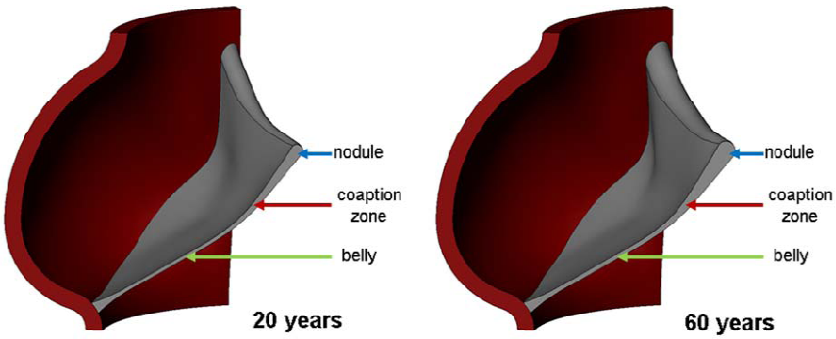

Figure 6 - Increased nodule thickness of the aortic valve leaflets with age (adpated from Weinberg 2009)

1.2 - Aortic Valve Replacement

The only effective treatment for aortic stenosis is surgical intervention to either cut adjacent joined leaflets or completely replace the valve. Valve replacement therapies were introduced in the 1960s and were performed as open heart surgery. A newer technique

called percutaneous or transcatheter aortic valve implantation (TAVI) involves threading a compressed replacement valve through a catheter into the aortic root and expanding the valve in place. During TAVI a balloon catheter is inserted through a femoral or internal jugular vein into the aorta or through the intercostals into the apex of the left ventricle (figure 7,8) [7, 8]. TAVI has become popular in Europe, but has not yet received FDA approval for use in the United States. The prospect of non-surgical intervention is appealing, and a recent follow up study of 358 patients 1 year after either TAVI or surgery showed a mortality rate of 30.7% for TAVI and 50.7% for surgery [9]. While a 20% higher survival rate may appear dramatic in such a large sample, the patients in the study were chosen because they were not considered suitable candidates for surgery. All patients in the study were severe cases, which does not imply the procedure would be as successful in TAVI cases with surgically viable patients. Additional studies indicate moderate success in patients who are not suitable for aortic valve surgery. Of 339 non-surgical candidates who underwent a TAVI with either a transapical or transfemoral approach, mortality rate was 22.1% after 8 months [10]. A study of only transapical procedures, 3 years post-procedure, on 71 patients found a survival rate of 69.8% for the 59 patients in the study who survived at least 30 days [11].

There are currently two major TAVI manufacturers: Edwards Lifesciences (Irvine, CA), which makes the SAPIEN valve, and Medtronic (Fridley, MN), which makes the CoreValve system[12] . Both valve systems can be implanted using transapical (figure 7) or transfemoral (figure 8) delivery methods. Retrograde implantation methods are preferable to antegrade methods because of the complex paths necessary to reach the aortic valve [13]. The preferred implantation route for both valve manufactures is through femoral access, however fragile vessels, porcelain aorta or other complications may indicate non-femoral access is preferred.

The Edwards SAPIEN valve is made from bovine pericardium, is 14-16mm in height, and is available in 23 mm and 26 mm sizes. Because of its design, it must be implanted below the coronary ostia to prevent blockage. The valve is often implanted at a 50-50 ratio about the annulus, so imaging assessment must be performed prior to implantation to ensure the coronary ostia are at least 7-8mm above the annulus to prevent occlusion. When femoral access is not allowed, it is preferred to implant the SAPIEN valve transapically.

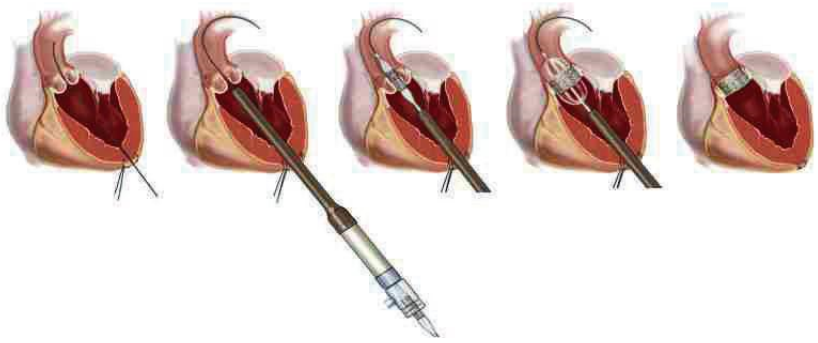

Figure 7 - Insertion and expansion of a replacement valve through the apex of the left ventricle (adapted from Routledge 2007)

Like the Edwards valve, Medtronic's CoreValve has a preferred femoral insertion approach, however it may be inserted through the subclavian artery is femoral access is not available. Because the valve stent is 50 mm in length, it extends beyond the valve's leaflets, which are made from porcine pericardium, and covers the coronary ostia. However, the ostia are not occluded because the stent is a coarse mesh, and only one or two stent wires may actually cross the ostia. Each valve has advantages over the other: SAPIEN is shorter in height and is very unlikely to occlude the coronary arteries, however the CoreValve's longer length gives it a larger to surface area to adhere to the aortic root to prevent stent migration.

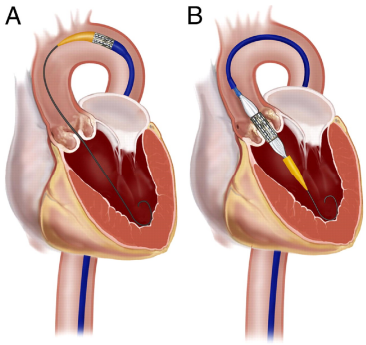

Figure 8 - Insertion of an Edwards replacement valve through the aorta, originating in the femoral artery (adapted from Webb 2009)

1.3 - Computational modeling

Modeling the aortic valve is critical to understanding the forces involved in valve expansion and placement, since the replacement valve relies on largely friction to retain its position until the tissues of the aortic root grow and adhere to the new valve. Patient-prosthetic mismatch (PPM) can be problematic and cause loose and shifting valves, which can be fatal if not corrected [14]. PPM can be reduced by simulating a valve/stent interaction. Computational modeling derived from imaging data allows a valve to be virtually placed inside a simulated aortic root specific to a patient. Any interactions between the new and existing valve can be observed and corrected before the actual procedure begins.

Stent expansive inside an existing valve is a complex, multi-step process. First, the stent must be expanded to size so it is firmly anchored in the tissue and cannot dislodge, but also cannot be over-expanded, which may cause tearing of the aortic root or annulus. Second, the original leaflets of the diseased valve must be pushed aside as the stent expands. If the leaflets are severely calcified, they may need to be cut and separated to allow the replacement valve to fit. Once leaflets are freely moving, they must be pushed aside as the stent is expanded. As the stent is expanded, the leaflets may bind on the side of the stent and fold, effectively creating two layers of existing valve behind the new stent. This extra

material may not allow the stent to fully expand or cause it to expand in an elliptical shape. A highly elliptical stent is not ideal because it allows paravalvular leakage [15].

Stent expansion can be modeled using finite element modeling (FEM) methods, which calculates the interactions of wire frame models. A FEM mesh is composed of hundreds of nodes joined by elements with inherent material properties such as thickness, strength, and flexibility. A mesh can also be allowed to deform under load by allowing elements to change length in relation to the force applied. Using image segmentation methods it is possible to extract a patient-specific mesh on which simulations can be run.

1.4 - Prior Valve and Imaging Research

1.4.1 - Aortic Valve Imaging and Measurement

An early instance of CT valve imaging was performed in 1987 and was termed ultrafast computed tomography [16]. This method used ECG gating to acquire a single slice during specific times in the cardiac cycle. Current technology such as MDCT allows the capture of a 3D volume of the heart during the entire cardiac cycle. CT examination of the valves was not ideal prior to the availability of MDCT because only slice at a time could be acquired. With MDCT, a 2D slice in any direction could be derived from the 3D volumetric data. It was now possible to perform one scan and examine all valves and coronary arteries. Alternate modalities include transesophageal (TEE) and transthoracic (TTE) echocardiography, which were in use prior to the introduction of 64 slice MDCT. Echocardiography is often used for the primary assessment of valve disease because the procedures (TTE) are non-invasive and produce no ionizing radiation. It has been noted that there is a greater difference in measurements obtained from MDCT than those obtained from TEE or TTE measurements [17]. This study found that TEE and TTE measurements are closer in agreement to each other than to MDCT. The implication being that use of MDCT measurement, while in moderate agreement with TEE and TTE, is different enough to cause

a physician to alter the plans for TAVI procedure than if planning were performed with echocardiography. It also implies that choice of TEE or TTE assessment would not affect TAVI planning.

MDCT imaging of the aortic valve contributed to two significant areas of valve research: disease assessment and normal geometry. Several groups have examined the diagnosis of valvular disease from 64 slice MDCT images, and produced excellent reference images of normal findings and diseased valves [18-21]. Even an interesting case of a quadricuspid aortic valve was described, with detailed 3D volume renderings of the valve derived from 64 slice MDCT scans [22]. The much more common tricuspid aortic valve has been measured extensively using echocardiography, MRI, and MDCT, with detailed measurement methods included with each study. However not all measurements are in agreement, which seems to result from differing measurement methods, and it is not clear which method is best for assessing a valve prior to TAVI.

Certain studies have used purely sagittal and coronal views to assess valve dimensions. Because the long and short axes of the aortic root are rarely parallel to these anatomic planes, measurements obtained may be different than the real dimensions [23]. An improvement on sagittal and coronal view measurements is to reslice an image volume along the long and short axis of the aortic root. Often, two measurements are made on a 2D short-axis image: due to the circular or elliptical shape of the cross-section of the aortic root, one in the minor diameter and another on the major diameter of the ellipse. An alternate method is to measure the perimeter of the valve cross section and divide by 2π to calculate the radius. Additionally the area of the valve cross section can be obtained and the radius obtained by taking the square root of the area divided by π. One study in particular found no significant difference between diameters obtained from direct measure and

calculated from the perimeter when assessing the annulus in MDCT images [24]. This study did find a significant difference between diameters obtained from surface area and direct measurement. Using perimeter appears to be preferable for the SOV cross section because of the non-circular nature of the contour.

1.4.2 - Existing Image Analysis Methods

Several techniques are currently used to segment medical images and assist in identifying structures and boundaries. The simplest method for medical image segmentation is based on pixel or voxel intensity, where all pixels above or below a certain threshold are extracted. The method works well assuming uniform intensity distribution, but can become ineffective when images fade in intensity at the edges because of the image collection specifics of the modality. Once an image is thresholded, it can be transformed into a surface which removes the blockyness of the voxels. An early method called marching cubes became very popular because of its effectiveness at creating surfaces from medical images [25]. Its basis is to create a surface or surfaces within a voxel based on how the intensity of that voxel compared to the surrounding voxels.

To overcome the problem of intensity variation across an image, a simple method called active contour models, and sometimes also called snakes, was developed [26]. This method allowed a line to iteratively deform to fit an image feature. Line fitting was done by extending a perpendicular line to the current line and finding the point along that line that contains the largest difference in intensity between two adjacent pixels.

Snakes were effective at feature fitting regardless of global intensity variations, however they did not find features based on shape, instead they only found differences in local intensity. If the objective of the algorithm was to find a specific shape among an image full of shapes, it had no prior information on which to base its search, and was not effective

at finding specific shapes. Tim Cootes developed an extension to snakes called active shape models, which took existing shape information into account when deforming the contours used in the snakes algorithm [27, 28]. Training involved manually identifying landmark points in a set of training images, where the same landmark referred to the same anatomical location on each training image. From this a point distribution model was created which contained information about the variability of the shapes. Using the snakes concept of finding internal image boundaries, the shape model would only deform in a manner consistent with the training data. Cootes later extended his ASM method to include local texture information when training and searching, which he termed active appearance models (AAM) [29]. Instead of searching for boundaries, the algorithm searched for areas of texture that matched the training data. This method is now commonly used in facial recognition and has proved effective in medical image analysis [30-34].

1.4.3 - State-of-the-Art segmentation of the aortic valve

The aortic valve and surrounding structure is complex, especially with dynamic leaflets, so simple thresholding is not effective at capturing details of the leaflets. Thresholding is effective in defining the shape of the valve root (sinuses) and the ascending aorta, especially when contrast agents are used during the exam. Bright blood images become very easy to threshold and apply a marching cubes algorithm to extract a valve surface. For faint structures, such as leaflets, the thresholding is not as effective, and local voxel information must be taken into account when attempting to find these boundaries. The local methods used in snakes, ASMs, and AAMs are ideal for this type of boundary detection.

With recent advances in computational power, the time necessary for algorithms to iteratively fit a surface is greatly reduced. A 1996 study of deformable surfaces found it took an average of 10 minutes to fit a mesh model to the inside surface of the left ventricle [35]. A

2010 study fit models to the aortic and mitral valves with an average computational time of 4.8 seconds [36]. As the computational power increases, more complex algorithms can be applied.

Early experiences in valve modeling were focused on creation of a standard valve model on which finite element methods (FEM) could be applied. A 2003 paper describes a mitral valve model which was created and simulated stresses applied [37]. As a proof of concept, a group created a computer model of a surgical replacement valve using a coordinate measuring machine [38]. This apparatus used a laser to scan the surface of a replacement valve, and a mesh model was created from the scanned point cloud. This method can be used to digitize valves from cadavers, however *in vivo* imaging methods are preferable because they can actually help the patient being imaged.

Once generic models became more commonplace, it became important to create patient-specific models. Several groups used active appearance and active shape models to segment the left ventricle, with one in particular using 3D ASM to segment cardiac MRI [34]. Van Assen et al overcame one of the largest problems with 3D ASM and AAM model training: the manual identification of landmarks. The change from 2D to 3D ASMs greatly increases the amount of work necessary to perform landmarking because not only does the number of points increase dramatically, but landmarks do not always occur on the same slice plane in each image. To attempt to make it easier to perform training, van Assen first aligned and scaled all the images in the training set to a template image. Anatomical landmarks were then selected on the template image and the scaling/aligning transformation in inverted to propagate the landmarks to all of the training images, thus semi-automatically landmarking all of the training data. From there, standard ASM methods can be used to build a PDM and perform target searching. A similar method of landmark

propagation originally developed by Frangi et al (2002) was utilized by a group not to segment the ventricles, but instead to classify the images by disease type [39, 40].

Segmentation of the ventricle is a common application for ASM and AAM methods, possibly because of the simple cone/bowl shape of the ventricle. A group from Yale University used a technique they called subject specific dynamical model (SSDM), a derivative of AAMs, to segment the left ventricle from cardiac MRI images [41]. Also using cardiac MRI images, a separate group segmented the left ventricle using AAMs and wavelet transformations [42].

Perhaps the most interesting and relevant valve modeling research is that done by Ionasec et al who have modeled the aortic valve and extracted patient specific valve models from CT data [43]. In their 2008 paper, they describe a method of creating a standard valve model which is then deformed to fit patient specific CT images. A generic model of the aortic valve was created by using non uniform rational B-splines (NURBS) as shown in figure 9. Ionasec et al went further to transform the 3D model into a 4D model by adding a tensor product, which "introduces a temporal parametric direction" to the model. A probabilistic boosting tree (PBT) algorithm, which relied on a training database, was used to initially identify landmark positions in the target images. The PBT is similar to AAMs, but identifies probable landmarks using a classification method instead of simple boundary detection. Once the model landmarks are approximately fitted to the target, the surfaces between the landmarks is fitted using boundary detection and steerable features.

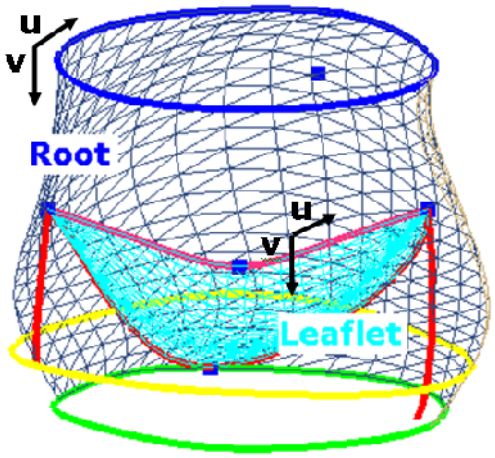

Figure 9 - NURBS model (adapted from Ionasec et al 2008)

Ionasec's group continued their work by expanding the model to include the mitral valve in a 2010 paper [36]. Using similar methods from their 2008 paper, they created a model of the aortic-mitral valve complex using 18 landmarks and interpolated surfaces between the landmarks. The target model estimation method was defined in three steps: 1) *global location* using PBT, marginal space learning (MSL), steerable features, and random sample consensus (RANSAC), 2) *non-rigid landmark motion estimation* using PBT and trajectory space learning (TSL), 3) *non-rigid shape estimation* using PBT, steerable features, and principle components analysis (PCA) based shape models.

Further expansion of this method was explained in another of the group's 2010 papers, which included 4D modeling of all four heart valves [44]. Their complete model consisted of 13 surface meshes and 35 landmarks (figure 10).

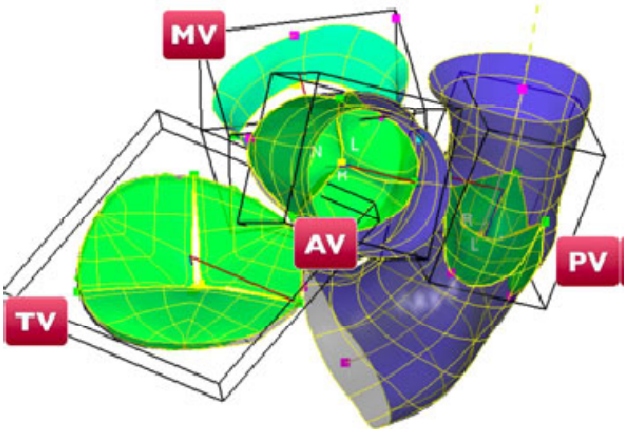

Figure 10 - Complete model of the heart valves: tricuspid valve (TV), mitral valve (MV), aortic valve (AV), and pulmonary valve (PV). (adapted from Grbic et al 2010)

1.5 - Our Approach

An overarching goal of this study is to create a computer model of the aortic valve based on the MDCT images obtained from a population of patients. To achieve that goal, we must understand our data and establish the methods necessary to create models of the aortic valve. Our objectives are: 1) Obtain aortic valve geometries from a large set of CT data using manual measurement methods to obtain variability of valve geometries. 2) Compare 2D manual measurements with 2D automatic measurements and 3D manual measurements. 3) Investigate the use of 3D active shape models to segment CT images on a patient-specific basis.

Gathering MDCT data is laborious but straightforward once methods are established to extract the data from a hospital picture archiving and control system (PACS). Manual 2D measurement utilizes standard radiological assessment methods, which are also laborious but create a ground truth to which other measurement methods can be obtained. Our automatic 2D measurement method uses a full width at half-max (FWHM) approach to detect edge boundaries and a simple algorithm to determine diameters. Our 3D measurement approach uses a commercial software application to create a 3D surface from segmented images and uses FE meshing software to manually measure geometries in 3D.

Finally, we investigate the use of statistical shape models to extract geometries. We are most interested in a variant of statistical shape models (SSM) called active appearance models (AAM), which segments images, especially valve leaflets, better than an intensity based segmentation algorithm. AAMs require a large amount of training data, which involves manually identifying hundreds of landmarks on multiple 3D images. We investigate a novel approach using high dimensional warping for landmark propagation to reduce the amount of manual training effort required. To date, no literature describes a computational model of stent-in-valve expansion, neither a generic model nor patient specific model. We hope to begin to address that issue using the work performed in this study.

2 – Methods

2.1 – Introduction to Methods

2.1.1 - Statistical Shape Models

Statistical shape models are based on the concept that an object has a certain shape, and regardless of the pose, scale, or position of the shape, the objects still retains the same basic shape. Combining a set of possible shapes of an object allows the creation of a statistical representation of an object's shape. An example is that of an arrow: each arrow contains 7 landmark points, which could be placed at the bends in the shape's outline (figure 11a). Arrows vary in size, rotation, and color, but all arrows have the same basic shape. When the shapes are aligned and normalized, statistics about the shape can be calculated (figure 11b). For example, after normalization the position of the tip of each arrow varies in relation to mean position of tip. The arrows in figure 11 can be considered training data, from which a model of landmark variability will be built.

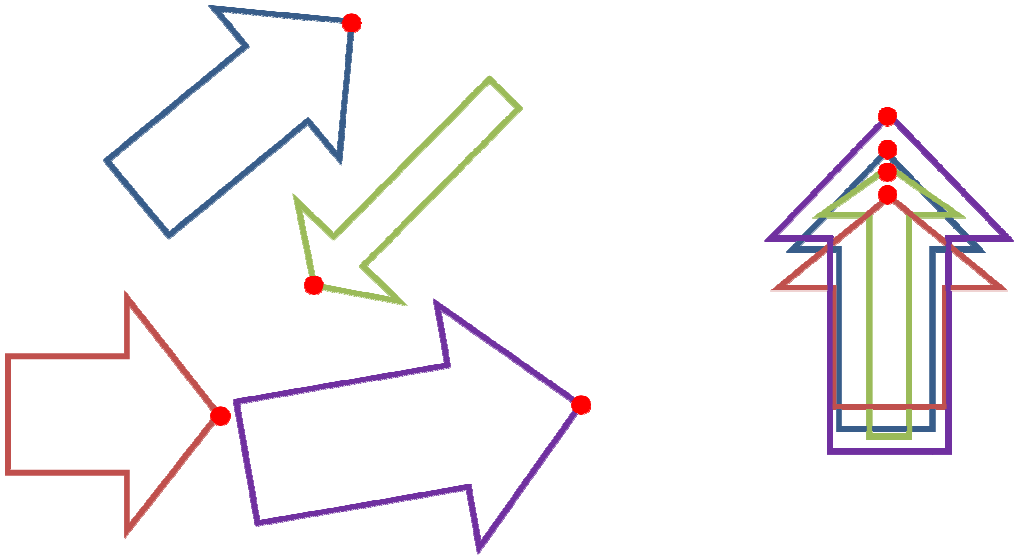

Figure 11 - (a) random shapes (b) aligned shapes

Using the variability of landmark position in the training data, a point distribution model (PDM) is created. This model represents how much each landmark point deviates from the mean shape, and in which direction it primarily deviates. After a PDM is created, a new shape can be created by changing a few parameters. This new shape can be compared to features in an image and an attempt at target matching can be made. The shape can be deformed iteratively until it best matches a target.

When matching a deformable model to a target, there are two costs involved: cost of matching and cost of deformation [45]. The cost of matching describes how well the model will match the orientation and position of the target. The cost of deformation describes how much the model must deform to fit the target. Cost of deformation also acts as a constraint on the matching cost because minimizing the deformation cost will prevent the template from forming implausible shapes. The best method is to minimize the sum of the deformation energy $E_d(\varphi)$ and matching energy $E_m(\varphi)$, where φ is the optimal vector parameter, and C is a weighting factor to control the deformation (all in 2D):

$$\min \xi\{E_m(\xi) + CE_d(\xi)\} \quad (1)$$

The deformation energy can be derived from a transformation where each model point is mapped using a continuous mapping function

$$(x, y) \rightarrow (x, y) + (D^x(x, y), D^y(x, y)) \tag{2}$$

where

$$D^x(x, y) = \sum_{m=1}^{M} \sum_{n=1}^{N} \xi_{mn}^x e_{mn}^x(x, y) \tag{3}$$

$$D^y(x, y) = \sum_{m=1}^{M} \sum_{n=1}^{N} \xi_{mn}^y e_{mn}^y(x, y) \tag{4}$$

$$e_{mn}^x(x, y) = \alpha_{mn} \sin \pi nx \cos \pi my \tag{5}$$

$$e_{mn}^y(x, y) = \alpha_{mn} \cos \pi mx \sin \pi ny \tag{6}$$

are the mapping functions and a normalizing constant is

$$\alpha_{mn} = \frac{1}{\pi^2 (n^2 + m^2)} \tag{7}$$

These can be used to describe the deformation energy

$$E_d(\xi) = \sum_m \sum_n ((\xi_{mn}^x)^2 + (\xi_{mn}^y)^2) \tag{8}$$

The matching energy can be described for an image *I* as

$$E_m(\xi, \theta, I) = \frac{I}{N_d} \sum_{i.j} (1 + \Phi(i, j)) \tag{9}$$

where θ is the set of parameters describing translation, rotation, and scale, and N_d is the number of contour points, and

$$\Phi(i, j) = -\exp(-\rho(\delta_i^2 + \delta_j^2)^{1/2}) \tag{10}$$

where ρ is a constant and (δ_i, δ_j) is the displacement of the (i,j) point from model to target [45].

2.1.1.1 - Active Shape Models

The simplest implementation of statistical shape models, called active shape models (ASMs) demonstrates the SSM concepts, and will be shown in the 2D version here. ASMs are primarily divided into a training step and a target searching step. Both steps are based on a point distribution model(PDM), which is a collection of points which describe variability of the training data [46-48]. The first step creates the PDM and the second step uses the PDM as a basis for segmentation. Training data is collected by initially specifying a point model and consistently applying that model to all of the shapes (structures) in the training data until a complete set of points is collected for all training data. During training, local gray level information is collected and stored for use during target searching (figure 12). Active appearance models (AAMs) record 2D texture samples instead 1D samples.

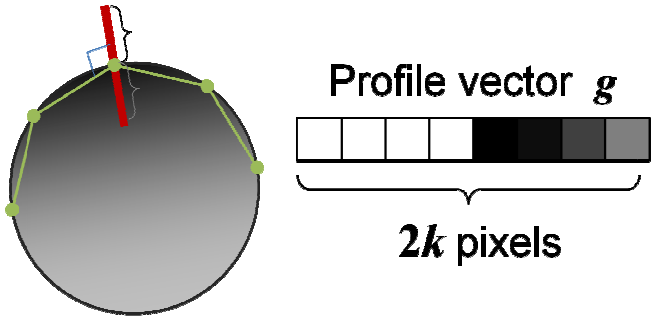

Figure 12 - (left) training image with landmark points in green. A tangent to the landmark contour is in red. (right) the gray level profile from the red line.

Training shapes are then aligned and placed into the same coordinate space using the Procrustes method [49]. The training shapes are realigned by aligning all the shapes to the first shape by minimizing the weighted sum

$$E = (\mathbf{x}_1 - M(s,\theta)[\mathbf{x}_2] - \mathbf{t})^T \mathbf{W}(\mathbf{x}_1 - M(s,\theta)[\mathbf{x}_2] - \mathbf{t}) \quad (11)$$

where x_1 and x_2 are the shapes to be aligned, θ is the angle of rotation, s is the scale, and (t_x,t_y) is a translation, and where

$$M(s,\theta)\begin{bmatrix} x_{jk} \\ y_{jk} \end{bmatrix} = \begin{pmatrix} (s\cos\theta)x_{jk} - (s\sin\theta)y_{jk} \\ (s\sin\theta)x_{jk} + (s\cos\theta)y_{jk} \end{pmatrix} \tag{12}$$

$$\mathbf{t} = (t_x, t_y, \cdots, t_x, t_y)^T \tag{13}$$

and **W** is a diagonal matrix of weights for each point *k*. The weight matrix is calculated by gathering statistics about each point and its relationship to all other points. Assuming R_{kl} is the distance between points *k* and *l*, and V_{Rkl} is the variance in this distance over the shapes for each point *k*

$$\mathbf{W}_k = \frac{1}{\left(\sum_{i=0}^{n-1} V_{R_{kl}}\right)} \tag{14}$$

The alignment process iterates through all shapes, aligning them to the first shape. The aligned shapes appear as a cloud of points when plotted. After alignment, statistics can be gathered about the training data, which will be used during feature extraction in the next step. To be able to fit a model to new target data, the model will need to be deformed and given an affinity for features in the target image, similar to way snakes seek out edges. However, ASMs will only be able to deform in a manner consistent with the training data, so constraints must be established that limit the deformation.

To deform the model in meaningful ways, the number of parameters used to change the shape must be reduced to a manageable number. If a model contained 100 points, it would require 100 parameters to deform the shape, which is a large number and individual point parameters are not very meaningful as feature information. This is done by applying PCA to reduce the parameter dimensionality and calculate a subset of eigenvectors which deform the model [50, 51]. The application of PCA will project a 2n dimensional space (number of points *n*, each point has 2 variables) onto an *M* dimensional space, thus reducing

the dimensionality. Assuming *N* shapes in the training set, the mean shape is calculated using

$$\bar{\mathbf{x}} = \frac{1}{N}\sum_{i=1}^{N}\mathbf{x}_i \tag{15}$$

Then the 2*n* x 2*n* covariance matrix **S** is calculated using

$$\mathbf{S} = \frac{1}{N}\sum_{i=1}^{N}(\mathbf{x}_i - \bar{\mathbf{x}})(\mathbf{x}_i - \bar{\mathbf{x}})^T \tag{16}$$

The unit eigenvectors of **S** are now described by $\mathbf{p}_k$, where

$$\mathbf{S}\mathbf{p}_k = \lambda_k \mathbf{p}_k \text{ and } \mathbf{p}_k^T \mathbf{p}_k = 1$$

The eigenvalues are described by λ_k (k = 1, … , 2n). The eigenvectors corresponding to the largest eigenvalues describe the most variance, and smallest eigenvalues describe the least. Describing all possible variance is not ideal because most of the eigenvectors actually cause little variability. Most variability in a model can be described by the 5-10 largest eigenvalues. To describe only the top *f* percent of the variance, the sum of *t* largest eigenvalues should be greater than or equal to the product of the total variance (V_T) and *f*, such that

$$V_T = \sum_{k=1}^{2n}\boldsymbol{\lambda}_k \tag{17}$$

$$\sum_{i=1}^{t}\lambda_i \geq f_v V_T \tag{18}$$

For example if 98% of the variance was used, *f* would be 0.98. The *t* largest eigenvalues and their corresponding eigenvectors are used to extract feature information when training and when classifying. Recall that the point distribution model equation for a new shape **x** is

$$\mathbf{x} = \bar{\mathbf{x}} + \mathbf{P}\mathbf{b} \tag{19}$$

where $\bar{\mathbf{x}}$ is the mean shape, **P** is a matrix of the *t* largest eigenvectors, and *b* is a vector of weights. The vector of weights defines the deformation for each new shape, and is used as the feature values in training and classification. The vector of weights collected during training will be used during classification.

When classifying a new shape, the modes of variation must be determined. This is done by searching a target image for a shape that can be matched to the point distribution model. Suitable points are found in the image that minimize the Mahalanobis distance between features of interest in the image and the model points, such that

$$f(\mathbf{g}_v) = (\mathbf{g}_v - \bar{\mathbf{g}}_p)^T \mathbf{S}_p^{-1} (\mathbf{g}_v - \bar{\mathbf{g}}_p) \tag{20}$$

where

$$\bar{\mathbf{g}}_p = \frac{1}{m} \sum_{i=1}^{m} \mathbf{g}_{pi} \tag{21}$$

is the mean vector containing local pixel information *g* from each point *p* of the model in the training data, and

$$\mathbf{S}_p = \frac{1}{m} \sum_{i=1}^{m} (\mathbf{g}_{pi} - \bar{\mathbf{g}}_{pi})(\mathbf{g}_{pi} - \bar{\mathbf{g}}_{pi})^T \tag{22}$$

is the covariance of that local pixel information.

Once new target points **Z** are found, the model **X** must be matched to those points such that the distance between target and model points is minimized. This is accomplished by iteratively realigning **X** to fit **Z** using the Procrustes method described previously, and determining the best weights *b* that deform **X** to fit **Z**. Once translation (X_t,Y_t), rotation (θ), and scale (*s*) parameters have been found using

$$\mathbf{X} = T_{X_t, Y_t, s, \theta}(\bar{\mathbf{x}} + \mathbf{Pb}) \tag{23}$$

where for a single point (x,y), the translation/rotation/scale function ($T_{X_t, Y_t, s, \theta}$) is

$$T_{X_t,Y_t,s,\theta}\begin{pmatrix} x \\ y \end{pmatrix} = \begin{pmatrix} X_t \\ Y_t \end{pmatrix} + \begin{pmatrix} s\cos\theta & -s\sin\theta \\ s\sin\theta & s\cos\theta \end{pmatrix}\begin{pmatrix} x \\ y \end{pmatrix} \quad (24)$$

the best weights must be found by minimizing the sum of squares distance between **X** and **Z**

$$\left|\mathbf{Z} - T_{X_t,Y_t,s,\theta}(\bar{\mathbf{x}} + \mathbf{Pb})\right|^2 \quad (25)$$

These new set of weights **b** define the feature information for that target image where **b** = (b_1, b_2, … b_t).

2.1.1.2 – SSM Training

Three dimensional statistical shape models are an ideal solution to our segmentation problem, however the manual effort required to landmark the training data is immense. An aortic valve model might contain 300 points, and training data might require 30 models, meaning 9000 landmarks must be manually selected in 3D. Selection of landmark points becomes even harder in 3D than in 2D because the person performing the landmarking must scroll through slices to find the anatomic location. This is extremely time-consuming when anatomies lie in different slices for different patients.

An ideal method would specify landmark points once and automatically propagate those points to all training images. Our novel method attempts to automatically propagate landmarks by creating a surface model from a template image once, and warp subsequent patient's data to fit the template model. Since all landmarks are known to correspond to the same anatomical location, the variability between the landmarks can be assessed. A mean FE model and the landmark's standard deviation, a point distribution model, can be calculated and this model can be deformed by changing its significant modes of variation.

Borrowing from the functional magnetic resonance imaging (fMRI) research in the neuroimaging field, high dimensional warping (HDW) can be used to warp a 3D gray-level volume to fit another 3D gray-level volume [52]. The need for 3D image warping came

about because brain shapes between patients are not identical, so each brain must be warped to fit a common template. Once all brains are in the same coordinate space, it can be assumed that the same anatomy occupies the same image coordinates in a group of patients that are to be compared to each other. We will use this method to attempt to simplify 3D SSM training.

2.1.2 - High dimensional warping

Creating patient specific finite element models of the aortic valve has become a trivial task with the introduction of 3D image segmentation software. A full mesh can be created in minutes from medical images once parameters and a seed point are specified. As noted before, automatic segmentation has drawbacks because valve leaflets are not accurately segmented using this method and more importantly model landmarks cannot be directly compared.

Our intention was to use HDW to warp target images to a template image, from which landmarks would be propagated, thus simplifying the 3D landmarking process and creating potentially more accurate landmarks than were obtained in van Assen's 2006 paper [34]. We sought to use the HDW toolbox from the Statistical Parametric Mapping (SPM) software package to 3D cardiac CT volumes [53, 54]. The HDW warping tool was primarily developed by John Ashburner to fit high resolution brain MRI images to a common template. The HDW toolbox is presented primary as a black box when using it in practice, however it is helpful to understand what is happening when running the tool, and is best understood when using a 2D example.

HDW uses a *maximum a posteriori* (MAP) approach to estimate a deformation field from image **a** to **b** and from **b** to **a** [54]. In principle each deformation field must be the

inverse of the other. The first step to non-rigid registration of two images begins with a Bayesian framework described by

$$p(\mathbf{Y} \mid \mathbf{b}) \propto p(\mathbf{b} \mid \mathbf{Y}) p(\mathbf{Y}) \tag{26}$$

where $p(\mathbf{Y})$ is the *a priori* probability of parameters **Y**, $p(\mathbf{b}|\mathbf{Y})$ is the probability of data **b** given parameters **Y**, $p(\mathbf{Y}|\mathbf{b})$ is the probability of parameters **Y** given data **b**, **Y** are the parameters to deform the image, and **b** are the images. The *maximum a posteriori* estimate is the value of **Y** that maximizes $p(\mathbf{Y}|\mathbf{b})$.

Prior potentials are calculated by considering the pixels of the image to be the nodes of a regular grid, with a triangular mesh between them. There is considered to be a uniform affine mapping between the images within each triangle. A 3x3 affine mapping **M** between triangles in images *x* and *y* can be obtained by:

$$\mathbf{M} = \begin{bmatrix} m_{11} & m_{12} & m_{13} \\ m_{21} & m_{22} & m_{23} \\ 0 & 0 & 1 \end{bmatrix} = \begin{bmatrix} y_{11} & y_{12} & y_{13} \\ y_{21} & y_{22} & y_{23} \\ 1 & 1 & 1 \end{bmatrix} \begin{bmatrix} x_{11} & x_{12} & x_{13} \\ x_{21} & x_{22} & x_{23} \\ 1 & 1 & 1 \end{bmatrix}^{-1} \tag{27}$$

A Jacobian matrix **J** of the affine mapping can be obtained by:

$$\mathbf{J} = \begin{bmatrix} m_{11} & m_{12} \\ m_{21} & m_{22} \end{bmatrix} \tag{28}$$

with a penalty for each triangle, where *s* is the area of the triangle and λ is a regularization parameter:

$$h = \lambda(1 + |\mathbf{J}|)(\log(s_{11})^2 + \log(s_{22})^2) / 2 \tag{29}$$

The prior potential of the whole image, $H(\mathbf{Y})$, is the sum of these penalties:

$$H(\mathbf{Y}) = \sum_{i=1}^{I} h_i \tag{30}$$

The set of parameters Y that describes the warping field are iteratively estimated by:

$$y_i^{(n+1)} = y_i^{(n)} - \varepsilon \frac{\partial H(\mathbf{Y} \mid \mathbf{b})}{\partial y_i} = y_i^{(n)} - \varepsilon \left(\frac{\partial H(\mathbf{b} \mid \mathbf{Y})}{\partial y_i} + \frac{\partial H(\mathbf{Y})}{\partial y_i} \right) \tag{31}$$

where *n* is the iteration number, *i* is the element number of **Y**, and ε is a small number. Essentially this iterative process moves the nodes in the direction that minimizes the *a posteriori* potential.

A simple 2D example illustrates the warping of one image to another and the corresponding deformation field (figure 13). The HDW toolbox writes out 4D Jacobian determinant images which can act as lookup tables to determine the backwards warping of image coordinates. In principle this kind of deformation is ideal for landmark propagation and subsequent use of the landmarks in a point distribution model.

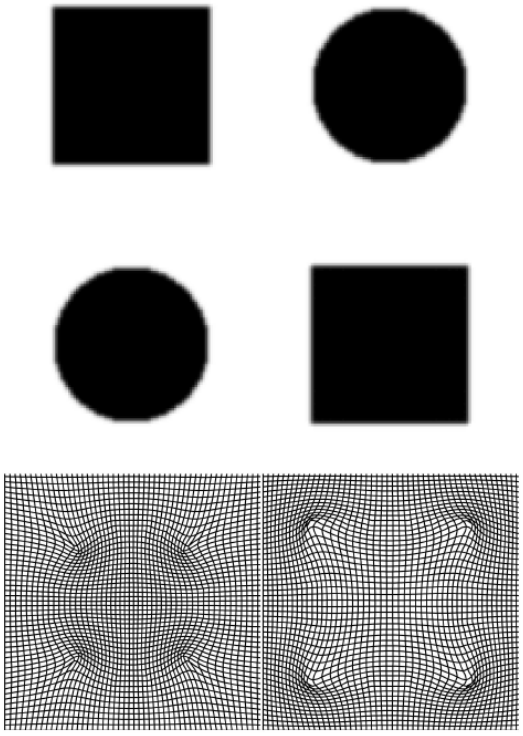

Figure 13 - 2D warping example. (left column) warping a square to fit a circle (right column) warping a circle to fit a square

2.2 - Implementation

At the start of this study, no 3D ASM or AAM implementations were readily available. Zambal et al implemented a 3D AAM of the left ventricle, however the work was sponsored by industry and thus the code was not released [55]. Though source code was not available, we were able to extract some important information about model building from Zambal's thesis.

Our implementation consisted of image importation, 3D measurement comparison, and began training of the deformable shape models using coordinate mapping and high dimensional warping. We did not yet implement 3D shape searching, which would require an extension of the 2D SSM methods. Shape searching may yield better results as more shapes are added to the training data. Since our HDW method produced semi-accurate estimates of valve shape, the results produced from it can be considered a starting point for additional training data. A boundary searching algorithm may produce more accurate representation of shape during training than either manual landmarking or warping. The accuracy of the training data may be improved by including models created by boundary detection and excluding inaccurate HDW models from the training, essentially building a database of shapes known to be accurate.

2.2.1 – 3D point picker

At the outset of this study, no suitable programs were available to assist with manual measurement, point cloud creation, or display of surfaces on images. We wrote a program initially to allow manual measurement in 3D images, and it was expanded to include point cloud picking and surface/volume display. It is now an open-source project available through Sourceforge.net (https://sourceforge.net/projects/vtkpointpicker). VTKPointPicker was written in C++, utilizing wxWidgets and VTK libraries. The primary interface displays the x,y,z planes of a 3D DICOM volume. Slices can scrolled through using

the mouse or buttons on the interface. Slice planes can be changes to any arrangement, which allows effective reslicing in the short and long axis of the aortic valve. VTKPointPicker can be run in batch mode when loading multiple studies for measurement, and has hotkeys which allow snapshots of the resliced planes to be saved in the portable network graphic (.png) format. Later versions of the program allowed Abaqus format FE files to be displayed in the same space as the resliced DICOM image data, allowing visual comparison of model fit.

2.3 - Data Collection

Institutional review board (IRB) approval was granted to analyze 64-slice multi detector-row CT (MDCT) images collected on patients scanned at Hartford Hospital between 2005 and 2010. Patients received MDCT scans because of suspected cardiac disease and thus scans were not ordered for the evaluation of the cardiac valves. Following acquisition of scans from the CT scanner, the images were stored on a PACS system and later retrieved in DICOM format for analysis. Though several CT sequences were collected, only the ECG gated full phase scan was used in our analyses.

MDCT exams were performed on a 64-slice GE Medical Systems Light Speed 64 channel VCT scanner (GE medical systems Milwaukee Wisconsin, USA) located at Hartford Hospital in Hartford, Connecticut. Patients received Ultravist, Isovue, or Visipaque contrast agent during their scans.

Prior to MDCT angiography, prospective calcium score acquisition was performed (DFOV 25 x 3.0 mm, rotation time 375 ms, voltage 120 kV, and tube current 500 mA). The temporal window was set at 75% interval after the R wave for ECG triggered prospective reconstruction. Calcium scoring was performed on a dedicated workstation. For MSCT coronary angiography a collimation of DFOV 25-30 x 0.625 mm and a rotation time of 375

ms were use resulting in a temporal resolution of less than 200 ms. The tube current modulation was automated to a maximum of 800 mA at 120 kV. Images were obtained with helical scanning and ECG gating. A timing bolus of 20 cc bolus of Ultravist 370 contrast (Bayer Healthcare Pharmaceuticals, Wayne NJ) was administered follow up with a 20 cc bolus of normal saline. A 1 second axial scan with a 1 second inter scan delay with a region of interest at the level of the ascending aorta were obtained until contrast density detected. 80 cc of Ultravist 370 contrast was administered via the antecubital vein at a flow rate of 5.0 mL per second using a Medrad Stellant dual headed injector and (Warendale, PA). (60 cc bolus of contrast, followed with a 50 cc bolus of 40% contrast and 60% saline, followed by a 20 cc bolus of saline). Data acquisition was obtained during an inspiratory breath hold of approximately 6-8 seconds with ECG gating. Multisegment reconstruction for coronary analysis was performed at 0.6 mm slice thickness routinely at 75% interval with reconstructions at additional 5% intervals as required on a dedicated 3-D workstation. Multisegment for functional analysis including right and left ventricular morphology and valve morphology was reconstructed at 1.25 mm slice thickness throughout the cardiac cycle at 10% intervals (0-90%) on a dedicated 3-D workstation.

To measure the dimensions of interest in the valve datasets, only the 70% phase bin was used because the images are acquired during diastole and there is little motion occurring at that phase. Valve leaflets are consistently motionless in the closed position, allowing measurement of the coaptation height.

2.4 - Manual 2D Measurement

Considered the gold standard for medical image evaluation, 2D manual measurement has been used since the first X-ray films were produced. As medical image collection methods grew from X-ray to include MRI, CT, PET, ultrasound, the capability of electronic storage methods grew simultaneously.

We were interested in the following measurements: annulus diameter, sinus of Valsalva (SOV) diameter, diameter at the left and right coronary artery (LCA, RCA) ostia, aorta diameter, annulus to coaptation distance, annulus to SOV distance, annulus to LCA and RCA ostium distance, annulus to aorta distance, and coaptation length (figure 14).

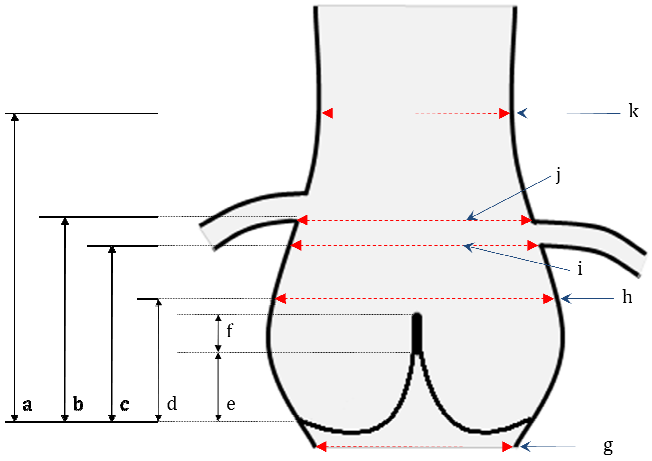

Figure 14 - Long axis view with diameters and heights indicated

To perform manual measurement, a short axis plane was first established on the aortic annulus by intersecting the bottoms of the leaflet-sinus attachments, which produced a plane approximately perpendicular to the long axis of the valve. Then, diameter and height quantities were measured for the structures of interest as the short axis slice plane was advanced, parallel to the annulus plane in 0.5mm slices, from the aortic annulus toward the ascending aorta.

Short axis measurement methods used in this study were similar to those used in previous studies [11, 14]. Two measurements were taken at each of diameter, one each along the major and minor axes (figure 4) of the cross-sections of the aortic root. Of note, the measurement of the annulus diameter was conducted on a plane approximately 0.5-1.0mm below the annulus to prevent leaflet edge effects from interfering with diameter

measurement (figure 3,4a). Perpendicular lines approximately equal to the shortest and longest diameters of the Sinus of Valsalva were measured at its widest point (figure 3,4b). Diameter was recorded at the plane intersection of the proximal portions of ostia of the LCA (figure 4c) and RCA (figure 4d) to the annulus. Aorta diameter was measured at the point above sinotubular junction where the aorta becomes circular.

All height measurements were based on the annulus plane (figure 14). The "Annulus to leaflet-coaptation" height was measured from the annulus to the bottom of leaflet coaptation line. Coaptation length was measured between the planes where the leaflets began and ended their central coaptation. Portions of ostia of the LCA (figure 4c) and RCA (figure 4d) proximal to the annulus were then located and heights were recorded. Ascending aorta height was recorded at the point above sinotubular junction where the aorta becomes circular.

The five short axis positions in figure 4 were saved as 2D images for each patient by the first CT reader using the VTK program. A second reader manually measured annulus, sinus, LCA, RCA, and aorta diameters from these 2D images using the same major/minor axis diameter method as the first rater used. The measurements obtained from the two readers were then averaged.

2.5 - Automatic 2D Measurement

An automatic segmentation and measuring program, written in Matlab (MathWorks, Natick, MA), was developed based on the full-width at half maximum (FWHM) approach [56], and used to automatically measure major and minor diameters, perimeter, and area on the five short axis images. Segmentation was first applied to the 2D images, which isolated the aortic valve body from the background. Briefly, a binary image was produced by thresholding, so that each pixel is classified as either valve or background according to its

gray level. Threshold was calculated for each image based on an intensity profile (Figure 15), which was extracted from a line in the 2D image (red line in Figure 16). Threshold was defined as the mean of the maximum and minimum pixel values along that line. All pixel values in the image higher than the threshold were now considered inside the valve and values lower than the threshold formed the boundary of the valve. From the thresholded image, the boundary of the aortic valve was extracted and the centroid was estimated. The longest diameter (major axis) was measured, as well as the diameter perpendicular to it, the perimeter, and area of the valve. Figure 16 shows an image of the aortic sinus with the segmented boundary and axis lines drawn.

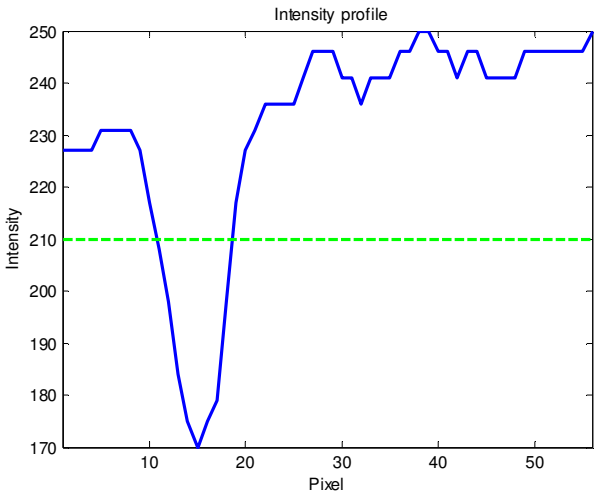

Figure 15 - Intensity profile across the red line in Figure 12

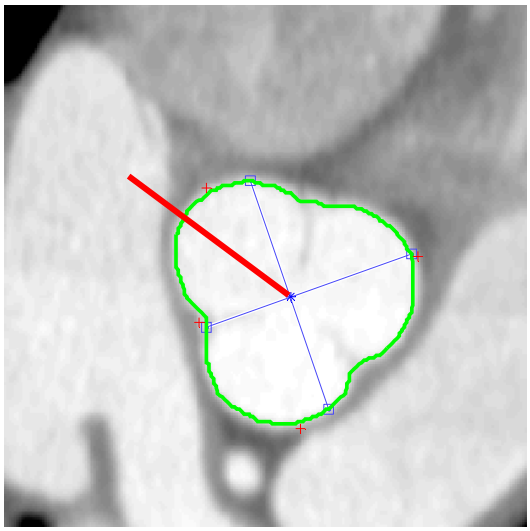

Figure 16 - Cross section of the aortic valve. Green line represents the boundary established by the FWHM segmentation approach. Blue lines represent the longest dimension passing through the shape centroid and corresponding perpendicular short dimension. Red line indicates the path from which the intensity profile is taken in Figure 11.

2.6 - Manual 3D Measurement

MSCT images were imported into the Mimics software for the 3D reconstruction. All patient images were evaluated using a window width of 950 Houndsfield units (HU) and -50 HU. Interior surfaces of the aortic root were automatically identified and separated from the rest of the chest images to create a 3D representation. Finite element (FE) surface mesh was

generated for the 3D aortic root model. The measurement of the aortic root was completed using the HyperMesh (Altair Engineering, Inc., Troy, Michigan, USA) software. The 3D FE mesh model was imported into HyperMesh. Landmark points (Figure 17) were selected from the model to identify the regions of the aortic annulus, the SOV, the sino-tubular junction (STJ), the aorta, and the coronary ostia (CO). For the diameter measurement of the annulus, STJ, and aorta, a total of 6 points were selected to highlight each height level (Figure 17). A closed smooth curve was interpolated using those 6 points. The generated smooth curve was assumed to be on the circumference of the region of interest and was used to calculate the diameter of each region. Additionally, sagittal and coronal projection measurements were calculated (figure 18).

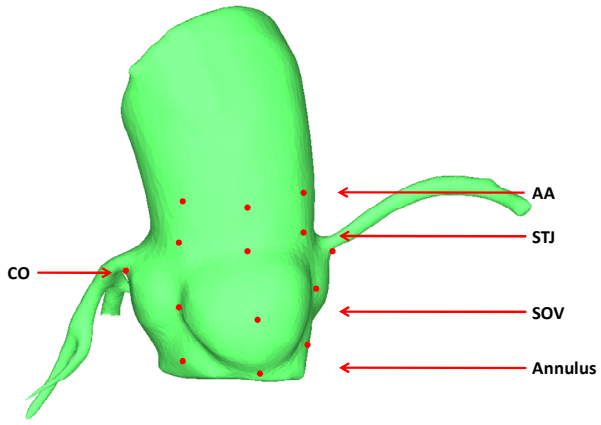

Figure 17 - 3D model derived from mimics segmentation data. (AA) ascending aorta (CO) coronary ostium (STJ) sino-tubular junction (SOV) sinus of Valsalva

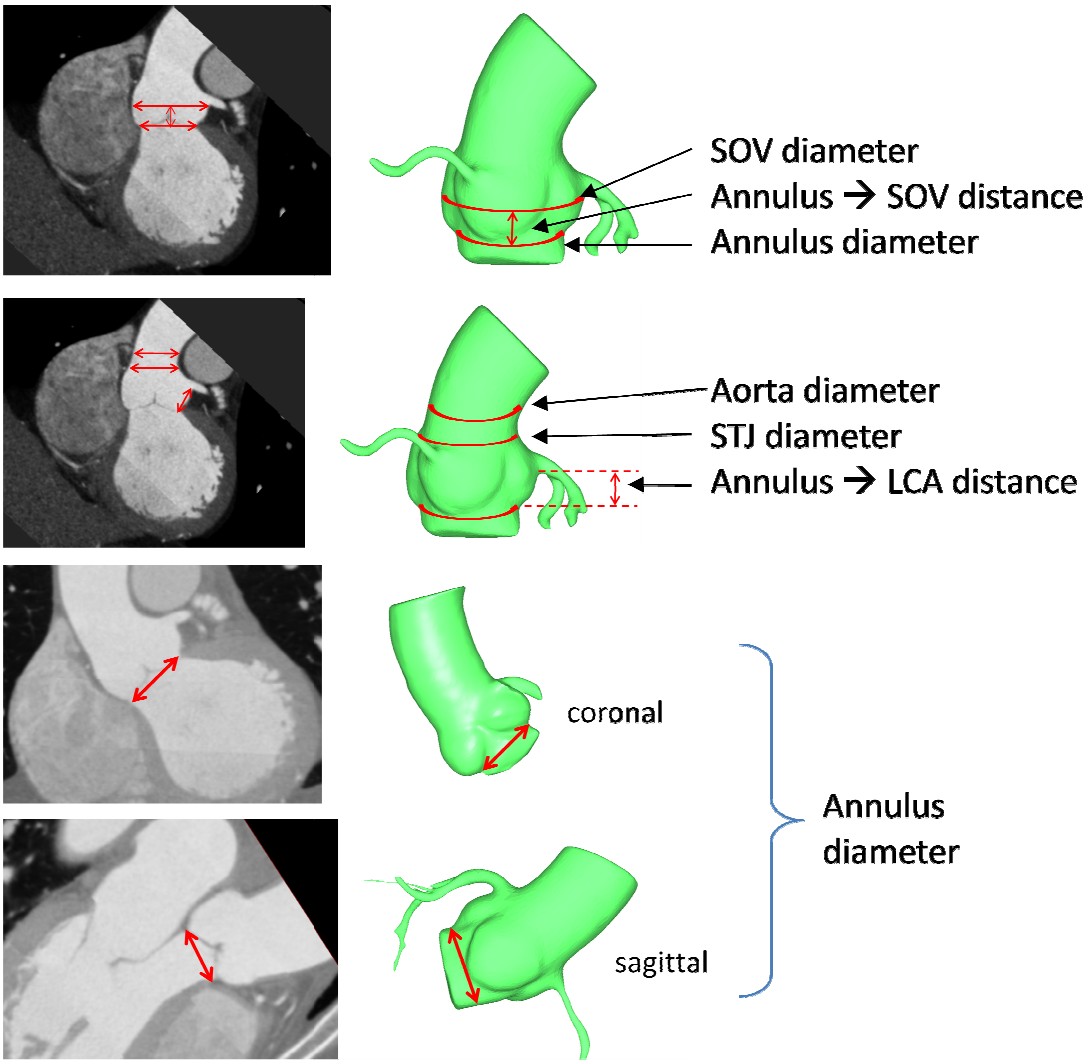

Figure 18 - Diameters, cross sections and coronal/sagittal projection measurements

2.7 - Measurement Comparison

To calculate the elliptical nature of the aortic valve, eccentricity ε, defined as

$$\sqrt{1-\left(\frac{b}{a}\right)^2} \tag{32}$$

where a and b are the major and minor axis lengths respectively, was calculated for all diameters in the 2D manual and automatic methods. To determine differences between the 2D manual and 2D automatic measurements methods, a paired t-test was used. In addition,

a less stringent test of percent difference was used to determine agreement between manual and automatic methods, which was defined as

$$abs\left(\frac{automatic - manual}{manual}\right) \tag{33}$$

where *abs* is the absolute value. Because of different sample sizes between 2D and 3D manual methods, an unpaired t-test was used to determine differences. An unpaired t-test was used to determine if measurements from the gender groups were significantly different. An ANOVA was used to determine if the measurements of the age separated groups were significantly different. All variables were reported as mean values with standard deviation and significance was determined by a p-value of 0.05 or less.

2.8 - Statistical Shape Models

Experimentation with a 2D cross section of the sinus and leaflets of the aortic valve demonstrates the results of creating a PDM and altering its b values to adjust shape. In this example, 5 tracings of the leaflets were recorded (figure 19) and a mean model was created. PCA was applied and a PDM was then created and its principle mode was varied (figure 20).

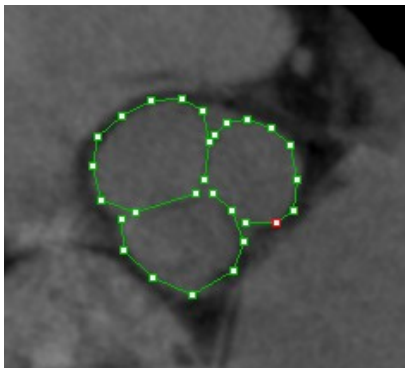

Figure 19 - Example 2D tracing of leaflets

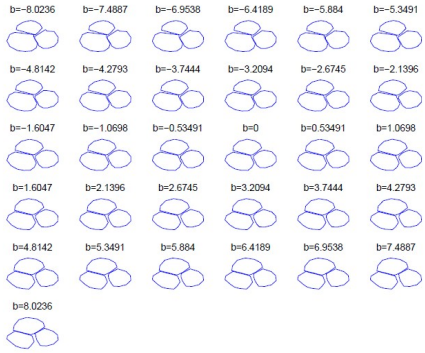

Figure 20 - Primary mode of variation for 2D example (varied between +/- 3 SD)

2.9 - High Dimensional Warping

2.9.1 – Template model creation

Using the VTKPointPicker, several hundred points were manually selected and recorded. The output was converted into Abaqus format and imported into HyperMesh. In HyperMesh, a model was built from the point cloud by creating smooth lines between nodes and meshing the surface. Surfaces were smoothed and edited; lines were split and joined, until the model accurately represented the valve in the template MDCT image. The surfaces were re-meshed to 4mm squares, resulting in a model with 1446 nodes. The aorta and coronary arteries were included originally included in this model, but were excluded to reduce the number of points for landmark propagation.

2.9.2 – Landmark propagation through warping/unwarping

MSCT images were manually loaded into an image viewer program and the center of the sinus of Valsalva located and recorded. Images were resampled to have isotropic voxels and were cropped to a sphere with a 40 mm radius centered at the centroid of the SOV (figure 23a). Manual coordinate picking allowed a rough alignment for all images before further processing, and cropping to a sphere reduced the amount of unnecessary information in the images. A template image was chosen from a 42 year old male patient who had an annulus diameter of 24.4 mm and a sinus diameter of 33.7 mm, which are

similar to the mean annulus and sinus diameters of 24.3 mm and 33.6 mm respectively for all 95 patients.

Using the realignment function in SPM8, the 94 target images were realigned to the template image and resampled into the same coordinate space. A maximum translation of 3.8 mm showed good prior alignment. After realignment, the images were warped to the template image using the high dimensional warping toolbox in batch mode, resulting in a 4D Jacobian determinant image describing the warping parameters to fit the target to the template (non-Jacobian image in figure 23b). Warping regularization was set to 0.75, with all other options staying as the default: bias correction and warping of 8 iterations, bias FWHM of 60mm and medium bias regularization. Warping regularization of 0.75 was chosen because the resulting warping was stronger than when using a default regularization of 4. The higher displacement necessary per voxel is most likely due to the size difference between a 200 mm brain and a 25 mm valve. The appropriate regularization was found by measuring the annulus diameter of a template and target, then warping the target to fit the template, unwarping the annulus measurements from the template to fit the template.

After warping, the previously created 1446 node mesh model of the template valve root was then unwarped using the Jacobian lookup table created in the previous warping step (figure 21). The unwarping step is described by using an example of template A and target B: B is warped to fit A, then selected landmark coordinates in A are unwarped into B's original coordinate space.

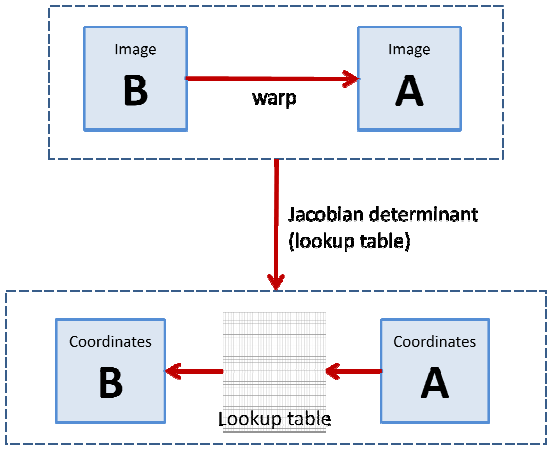

Figure 21 - Extraction of points from warped images. The warping of one 3D volume to another 3D volume produces a Jacobian image. This 4D image acts as a lookup table to find the inverse warp on specific Cartesian points.

The Jacobian determinant created during warping was stored as a triplet of 3D images. Each landmark coordinate in the FEM, x_{new},y_{new},z_{new}, was mapped from the Jacobian image using the following equations

$$x_{new} = Jacobian\left(x_{old}, y_{old}, z_{old}, 1\right) \tag{34}$$

$$y_{new} = Jacobian(x_{old}, y_{old}, z_{old}, 2) \tag{35}$$

$$z_{new} = Jacobian(x_{old}, y_{old}, z_{old}, 3) \tag{36}$$

where x_{old},y_{old},z_{old} are the template coordinates and 1,2,3 are the volume indices. Simply, the intensity value at coordinate *x,y,z* in volume 1 represents the unwarped *x* coordinate, the intensity value at coordinate *x,y,z* in volume 2 represents the unwarped *y* coordinate, and the intensity value at point *x,y,z* in volume 3 represents the unwarped *z* coordinate.

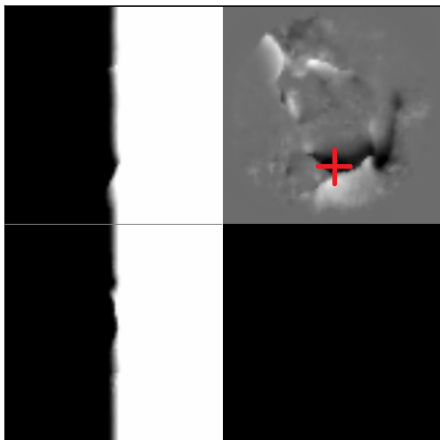

Figure 22 - Jacobian lookup table for the x coordinate. This is a view from the orthogonal view inside Mricro, coordinate position and intensity are displayed in the program.

An example of the Jacobian mapping is shown in figure 22: only the first 3D volume (x coordinate) is shown. The top-left panel of figure 22 is sliced across the x-plane, bottom-left is the z plane, and top-right panel is the y plane. In this example, coordinate [40 41 21], marked with a red crosshair, has an intensity value of 38.11 (obtained from Mricro). Since the x slice of the image is 40, it implies the x coordinate has shifted from 40 to 38.11, which is a warped displacement of 1.89mm in the x direction. This process is repeated for y and z coordinates, resulting in an inverse mapping. The process is also repeated for all coordinates in the template model, and for all models in the dataset. See Appendix B.1 for sample Matlab code.

Once new FE models are created for each image, the models can be combined into a PDM. Again, since each model has the same number of points and the points should now describe the same anatomical landmarks across patients, the mean shape and standard deviation of each landmark can be easily calculated. Models are aligned to the mean model using the Procrustes method and principle components analysis (PCA) is then applied to the model and eigenvectors and eigenvalues calculated [49]. A single variable can be now used to vary the mean model based on the most significant modes of variation [27].

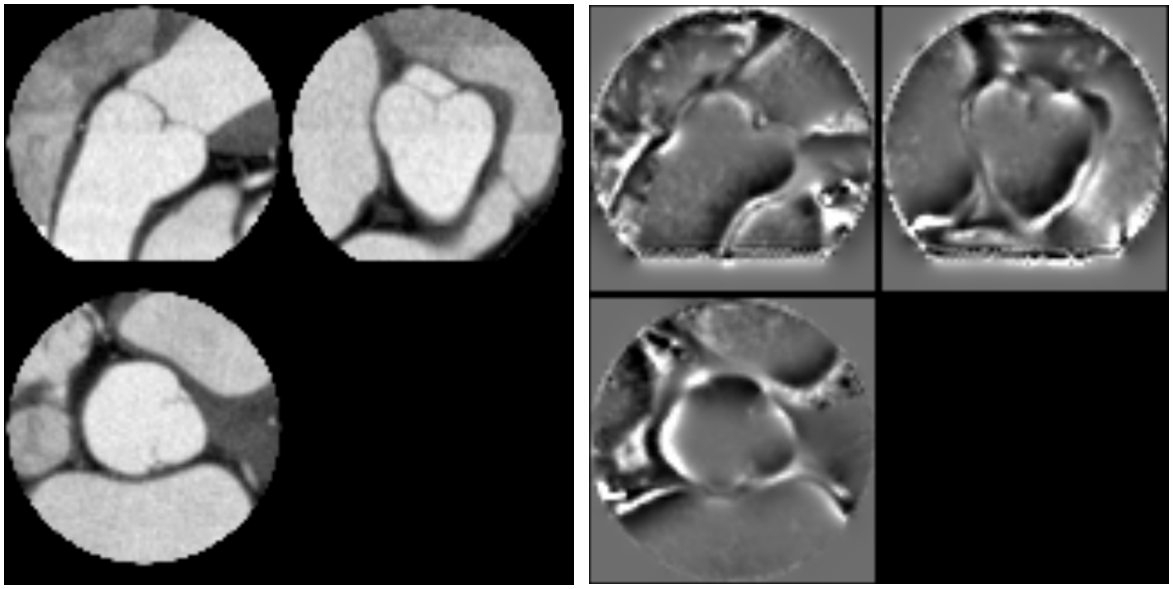

Figure 23 - (left [A]) spherically cropped valve, centered at the SOV (right [B]) deformation field, where light areas indicate expansion of voxels while dark areas indicate shrinking of voxels

2.9.3 - Verification of HDW Results

Measurements of known distances were taken from warped models, which included the two perpendicular distances measured across the annulus and two perpendicular distances measured across the sinus (figure 4b). Warped models were measured by calculating the distance between two nodes in 3D. Measurements from warped models were compared to manually acquired measurements using a paired t-test.

2.10 - Point Distribution Models

With 95 models that should approximate the variation between actual valves, PDMs can be created using standard 2D methods extended to 3D. Models are aligned to the first model using the Procrustes alignment method in 3D, which is implemented as MatLab's N-dimensional procrustes function (see Appendix B). Once aligned, a mean model can be created using equation (15). This mean model will later be the base model on which variation is added to create new models. Covariance is calculated on the aligned shapes

using equation (16), however it will produce a 3n x 3n covariance matrix because the models are 3D.

Eigenvectors and eigenvalues are calculated and the total variance is calculated using equation (17). The t most important eigenvectors are determined using equation (18). Now with a mean model and principle components defined, the mean model can be varied in a statistically meaningful way by varying the b vector in equation (19).

Five sets of PDMs were calculated to demonstrate the 3D additions to the PDM method. The first PDM was composed of all 95 models that resulted from the HDW. In theory these models should represent the actual dimensions of the valves in the images and be as close to the ground truth as possible. The second, third, and fourth PDMs were created from 42, 29, and 9 models respectively. Each set of models were grouped based on their similarity to the template dimensions. The second PDM was composed of only models which had manually measured annulus diameters of ±2 mm different than the template. In this way, the models can be considered 'annulus size-matched', which may compensate for the lack of deformation from the warping algorithm. The third and fourth PDMs were size-matched using the sinus and annulus&sinus dimensions respectively.

Since neither the 95 patient nor sized-matched PDMs had landmark variation of more than 2-3 mm, we wanted to test a method that artificially increased the variability between landmarks and see the results in a PDM. To compensate for the lack of large deformations, the third PDM was composed of models that were scaled in two dimensions. Using manually obtained measurements of the SOV diameter and annulus to aorta height, new models were created by scaling the template model. A scaling factor s_x was applied in the X and Y directions based on the ratio of SOV diameters of the target and template images respectively. A scaling factor s_z was applied in the Z direction based on the ratio of

the annulus to aorta heights of the target and template images respectively. Models were scaled in two directions to introduce variability that would not be removed during normalization of the models in the PDM creation. This step created 95 scaled models from which the fifth PDM was created.

PDMs were tested by varying the primary mode of variation between -5 and +5 standard deviations of the mean and new models created using equation (19).

3 - Results

3.1 - Study Population

Of the 116 patients selected for this study, 15 were excluded because of incomplete or poor quality MDCT images, aortic aneurysm, or prior valve implantation and six excluded because of severe aortic stenosis or bicuspid aortic valves. Severe aortic stenosis and poor image quality proved challenging for the automatic segmentation algorithm to assess, and were thus excluded from manual and automatic measurements. Of the 95 patients with no or mild aortic stenosis, 62% were male (36 female, 59 male) with a mean age of 57 ±13 years and a range of 16 to 85 years. Mean age of females was 58 ±12 years, and 57 ±13 years for males. Patient population characteristics and risk factors are listed in table 1.

Table 1 - Patient population statistics

	Population (n=95)
Age (years)	57.2 (±12.8)
Age range	16 – 85 years
Gender (M/F)	59 / 36
Mild stenosis	7
% w/diabetes	15
% w/hypertension	33
% smoker	10
% w/high cholesterol	24
Calcium score	146 ±251
LVEF (%)	64 ±7

3.2 - Manual 2D Measurement

Mean aortic annulus diameter was 24.4 ±2.7 mm for all 95 patients. Major and minor axes of the cross section of the annulus were 27.9 ±3.2 mm and 20.9 ±2.7 mm respectively, with a definite elliptical shape and an eccentricity of ε = 0.65. Diameter was measured as 33.5 ±4.7 mm at the sinus of Valsalva, 33.0 ±4.8 mm at the base of the left coronary artery (LCA) ostium, 31.9 ±4.6 mm at the base of the right coronary artery (RCA) ostium, and 29.6 ±4.5 mm at the aorta (table 2). Mean coaptation length was 2.5 ±0.7 mm, and height from the annulus to: coaptation, sinus, LCA ostium, RCA ostium, and aorta were 5.2 ±0.9 mm, 12.5 ±1.8 mm, 15.5 ±3.1 mm, 17.4 ±3.0 mm, 23.3 ±2.9 mm respectively (table 2). Distance between the level of the annulus and the LCA was less than distance to the RCA in 75% of patients. An ANOVA of the annulus, sinus, LCA, RCA, and aorta diameters showed the valve diameters to be significantly different, indicating the aortic valve is not a tube shape ($p < 0.0001$).

Table 2 - 2D manual diameter measurements

	2D Manual	
Diameter (mm)	**Mean**	**Eccentricity ε**
Annulus	24.4 ±2.7	0.65 ±0.08
Annulus major axis	27.9 ±3.1	-
Annulus minor axis	20.9 ±2.7	-
Sinus	33.5 ±4.7	0.42 ±0.12
at LCA	33.0 ±4.8	0.41 ±0.12
at RCA	31.9 ±4.6	0.35 ±0.14
Aorta	29.6 ±4.5	0.25 ±0.11

3.2.1 - Gender and Age Differences

Mean annulus diameter was 25.2 ±2.5 mm for males and 23.0 ±2.5 mm for females, indicating a statistically significant difference between genders. Mean diameter between genders was also statistically significantly different for sinus, LCA, RCA, and aorta, with males having significantly larger diameters. (Table 4 & Figure 25). A paired t-test indicated that only the annulus to aorta height was significantly different between males and females.

While annulus to sinus height and coaptation length were not statistically significantly different, a p-value of approximately 0.06 indicates a trend toward significance (Table 4). No significant differences in any measurements were found between age groups (table 3).

Table 3 – 2D manual measurement differences by age group

	Age				
Diameter (mm)	**<50 (N=26)**	**50-59 (N=29)**	**60-69 (N=26)**	**>70 (N=14)**	**ANOVA**
Annulus diameter	24.8 ±3.4	24.4 ±2.7	24.1 ±2.2	24.1 ±2.3	P=0.794
Sinus diameter	33.7 ±4.7	34.3 ±5.3	33.3 ±4.3	32.8 ±3.4	P=0.755
Diameter at LCA	33.1 ±4.9	33.3 ±5.4	32.8 ±4.1	32.4 ±3.9	P=0.940
Diameter at RCA	32.0 ±4.8	32.5 ±5.5	31.6 ±3.6	30.9 ±2.9	P=0.724
Aorta diameter	29.7 ±4.7	30.5 ±5.8	29.3 ±3.3	28.3 ±2.4	P=0.487
Height (mm)					
Annulus → leaflet coaptation	5.2 ±1.1	5.3 ±1.0	5.3 ±0.9	5.1 ±0.7	P=0.907
Coaptation length	2.3 ±0.6	2.6 ±1.0	2.5 ±0.7	2.5 ±0.6	P=0.544
Annulus → middle sinus	11.9 ±1.7	12.7 ±2.1	12.8 ±1.7	13.0 ±1.5	P=0.185
Annulus → LCA	15.9 ±3.2	15.4 ±3.5	15.5 ±2.9	14.9 ±2.5	P=0.809
Annulus → RCA	17.9 ±2.8	17.3 ±2.8	17.2 ±3.7	17.3 ±2.6	p=0.839
Annulus → aorta	24.1 ±3.5	23.2 ±2.8	23.1 ±2.8	22.6 ±1.9	P=0.408
% of patients with smaller distance to LCA than to RCA	73.1% (7.7% equal)	72.4% (3.4% equal)	73.1% (3.8% equal)	85.7%	-

Table 4 - Gender comparison for diameters and heights from 2D manual measurements

Diameter (mm)	**Male (N=59)**	**Female (N=36)**	**Unpaired t-test**
Annulus diameter	25.2 ±2.5	23.0 ±2.5	* P<0.0001
Sinus diameter	34.7 ±4.4	31.9 ±4.5	* P=0.0036
Diameter at LCA	34.2 ±4.4	31.1 ±4.5	* P=0.0014
Diameter at RCA	33.0 ±4.3	30.1 ±4.2	* P=0.0018
Aorta diameter	30.5 ±4.5	28.1 ±4.1	* P=0.0107
Height (mm)			
Annulus → leaflet-coaptation	5.3 ±1.0	5.2 ±0.8	* p=0.6123
Coaptation length	2.6 ±0.8	2.3 ±0.7	** p=0.0665
Annulus → middle sinus	12.8 ±1.9	12.1 ±1.5	** p=0.0632
Annulus → LCA	15.8 ±3.2	14.9 ±3.1	p=0.1817
Annulus → RCA	17.8 ±3.0	16.8 ±2.7	p=0.1053
Annulus → aorta	23.9 ±2.9	22.4 ±2.6	* p=0.0127
% of patients with smaller distance to LCA than to RCA	76.3% (3.4% equal)	72.2% (5.6% equal)	-

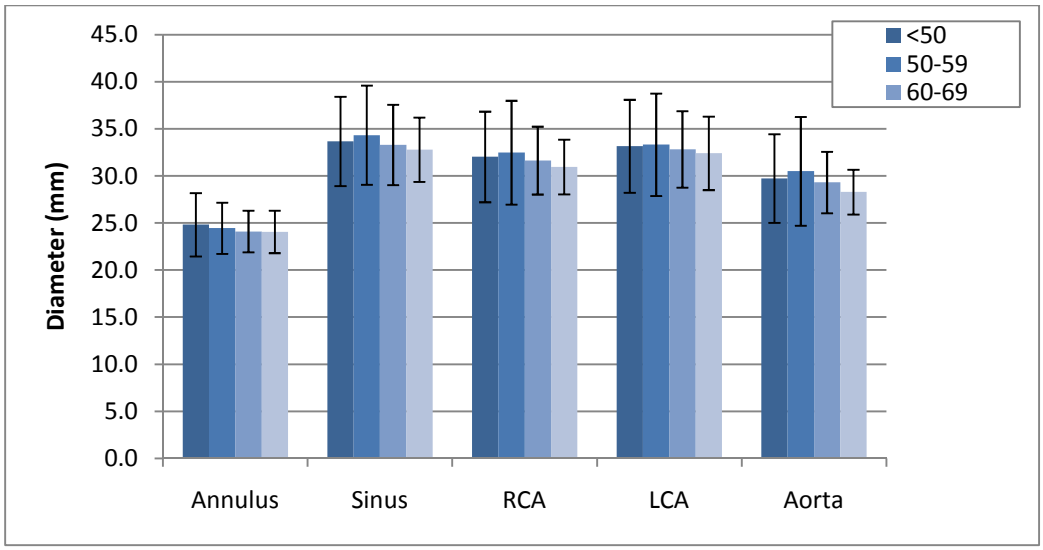

Figure 24 - Comparison of diameters by age from 2D manual measurements

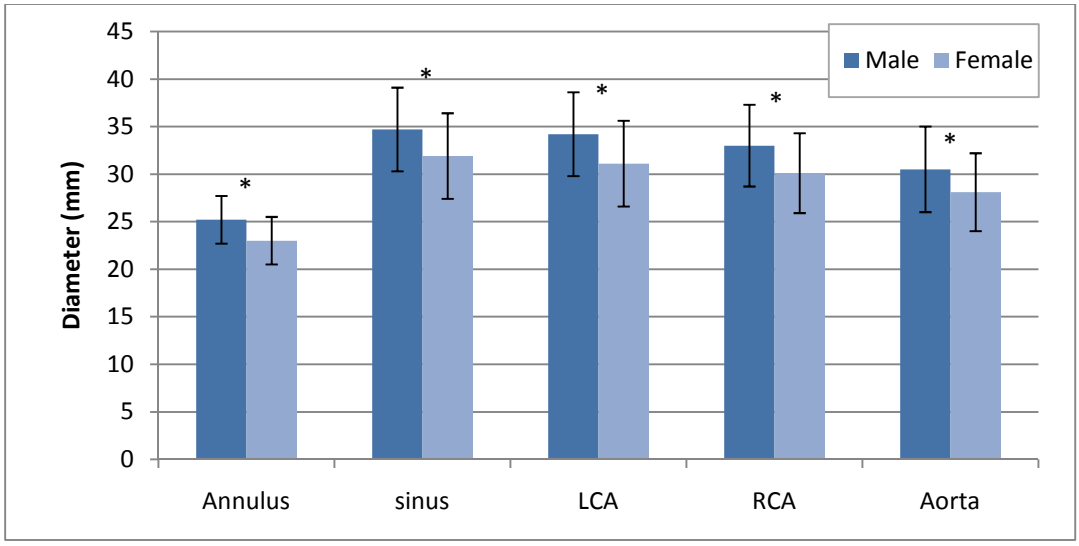

Figure 25 - Comparison of diameters by gender from 2D manual measurements

3.3 - Automatic 2D Measurement

The automatic algorithm was able to segment and measure 93 of the patient images, while 2 were not segmented because of low SNR. Mean annulus diameter from the automatic algorithm was 23.2 ±2.7 mm, with an eccentricity of ε = 0.65. Major and minor axes of the annulus were 26.5 ±3.0 mm and 19.9 ±2.7 mm respectively. Diameter was 32.9 ±4.6 mm at the sinus of Valsalva, 32.6 ±4.6 mm at the base of the left coronary artery (LCA)

ostium, 31.9 ±4.6 mm at the base of the right coronary artery (RCA) ostium, and 29.1 ±4.5 mm at the aorta (table 5).

Table 5 - Diameter measurements from 2D automatic method

	2D Automatic			
Diameter (mm)	Mean	Eccentricity ε	Perimeter	Area (mm^2)
Annulus	23.2 ±2.7	0.65 ±0.07	77.6 ±8.9	414 ±95
Annulus major axis	26.5 ±3.0	-	-	-
Annulus minor axis	19.9 ±2.7	-	-	-
Sinus	32.9 ±4.6	0.44 ±0.09	111.97 ±15.4	854 ±234
at LCA	32.6 ±4.6	0.47 ±0.09	108.3 ±15.8	847 ±227
at RCA	31.9 ±4.6	0.45 ±0.11	104.8 ±15.5	795 ±217
Aorta	29.1 ±4.5	0.33 ±0.09	95.0 ±14.9	674 ±216

3.4 - Manual 3D Measurement

Mimics was able to extract 3D models from 75 of the 95 patients (table 6). Annulus diameter was 24.7 ±2.7 mm, with coronal and sagittal axes of 25.9 ±3.1 mm and 22.5 ±2.4 mm respectively. Sinus of Valsalva diameter was 34.6 ±4.4 mm, and ascending aorta diameter was 29.9 ±3.6 mm. Height of the LCA ostium was 13.6 ±2.9 mm, and was 16.8 ±3.1 mm for the RCA ostium. Height of the sinus of Valsalva above the annulus was 15.8 ±2.1 mm.

Table 6 - Diameter measurements from 3D manual method

	3D manual	
Diameter (mm)	Mean	Area (mm^2)
Annulus	24.9 ±2.6	476 ±99
Annulus major axis	26.2 ±3.0	-
Annulus minor axis	22.7 ±2.4	-
Annulus coronal view	25.9 ±3.1	-
Annulus sagittal view	22.5 ±2.4	-
Sinus	34.8 ±4.3	-
Aorta	30.0 ±3.6	-

3.5 - Measurement Comparison

A paired t-test between 2D manual and 2D automatic methods indicated significant difference between annulus diameter, including major and minor axes, but no significant

difference between sinus, LCA, RCA, and aorta diameters (table 9). Percent difference was found to be highest, at 5.0%, for the annulus diameters, and lowest, 0.1%, for diameter at RCA. A paired t-test between 2D manual and 3D manual indicated significant differences in all measurements (table 9). Bland-Altman plots for difference in annulus measurements showed narrower range of differences between the 2D manual and automatic methods (±2 SD 2.9 mm), but a mean of -1.2 mm. Agreement between 2D/3D manual measurements showed a wider range of difference (±2 SD 4.95 mm), but a mean of 0.35 mm.

Table 7 - comparison of annulus diameter from the three methods

Diameter (mm)		2D Manual (n=95)	2D Automatic (n=93)	3D Manual (n=75)
Annulus	From perimeter	-	24.7 ±2.8	24.7 ±2.7
	Major Axis	27.9 ±3.1	26.5 ±3.0	-
	Minor Axis	20.9 ±2.7	19.9±2.7	
	Coronal View	-	-	25.9 ±3.1
	Sagittal View			22.5 ±2.4

Left coronary ostia heights were significantly different between 2D manual and 3D manual measurements, but not significantly different for right coronary ostia height (table 8).

Table 8 - Coronary ostia height comparison by method (* indicates significant difference)

Height (mm)	Mean (2D Manual) n=95	Mean (3D Manual) n=75	P value
Annulus → LCA	15.5 ±3.1	13.6 ±2.9	p<0.0001*
Annulus → RCA	17.4 ±3.0	16.9 ±2.0	p=0.2161

Results in table 7 and table 9 show that perimeter measurements from 2D automatic and 3D manual methods were not significantly different for the calculation of the annulus diameter.

Table 9 - method comparison for all diameters, with perimeter/direct comparison

Diameter (mm)	2D Manual / 2D Auto (n=93) Paired *t*-test	2D Manual / 2D Auto (n=93) % Difference	2D Auto Direct Measurement/ Perimeter (n=93) Paired *t*-test	2D Auto Perimeter / 3D Manual Perimeter (n=75) Paired *t*-test
Annulus	-	-	p<0.0001*	p=0.551
Annulus Major Axis	p=0.002*	5.0%	-	-

Annulus Minor Axis	p=0.010*	4.9%	-	-
SOV	p=0.337	1.9%	p<0.0001*	p<0.0001*
at LCA	p=0.580	1.2%	p<0.0001*	-
at RCA	p=0.952	0.1%	p<0.0001*	-
AA	p=0.401	1.9%	p<0.0001*	P=0.906

Comparison between this and other studies showed our 2D manual measurement results were consistent with previous literature (table 10). Tops et al used the coronal/sagittal slice plane to measure, while all other groups used oblique. Akhtar et al's measurements of ostia height were very different than our results and those of other studies.

Table 10 - Comparison of 2D manual measurements from this study to previous studies

	Current Study	Wood [57]	Tops [23]	Messika-Zeitoun [17]	Schultz [24]	Stolzmann [58]	Akhtar [59]
Patient demographics							
N	95	26	150	45	75	100	25
% Male	62%	-	65%	58%	51%	56%	56%
Age	57 ±13	82 ±9	54 ±11	80 ±8	81	61 ±9	76 ±7
Diameter (mm)							
Annulus	24.4 ±2.7	(23.5)	(24.85)	24.6 ±2.4	24.1 ±2.6	23.0 ±3.1	27.2 ±4.0
Annulus (short)	20.9 ±2.7	21.5 ±2.1	23.4 ±2.7	21.7 ±2.3	21.4 ±2.8	-	-
Annulus (long)	27.9 ±3.1	25.5 ±2.5	26.3 ±2.6	27.5 ±3.1	26.9 ±2.8	-	-
Sinus of Valsalva	33.6 ±5.1	32.5 ±3.0	32.3 ±3.9	-	-	33.5 ±4.2	36.7 ±5.3
Sino-tubular Junction	-	-	28.1 ±3.1	-	-	25.9 ±3.3	28.2 ±4.7
Height (mm)							
Annulus → middle sinus	12.5 ±1.8	-	17.2 ±2.7	-	-	-	-
Annulus → LCA	15.5 ±3.1	15.0 ±3.0	14.4 ±2.8	-	-	14.9 ±3.2	15.7 ±2.6
Annulus → RCA	17.4 ±3.0	-	17.2 ±3.3	-	-	16.8 ±3.6	15.6 ±2.7

3.6 - High Dimensional Warping

3.6.1 – Template model creation

Creation of the template model took approximately 40 hours by an experienced HyperMesh user. Manually selecting landmarks from VTKPointPicker took approximately one hour. Landmark points were not selected based on anatomic location, i.e. they were not selected to conform to a common template where point *n* always refers to anatomic location *x*. Because of random landmark placement, the amount of time needed to landmark the template was significantly less than the method traditionally used for SSM training.

3.6.2 – Warping results

When comparing annulus and sinus measurements of all 95 warped models to their manually measured values, annulus diameter was significantly different, while sinus diameter was not. When grouping subjects by similar annulus size, in the range of 24.2 – 28.2 mm, both annulus and sinus diameters were significantly different. By grouping subjects by similar sinus size (29.2 - 33.2 mm) it was found that measurements obtained by warping and manual measurements were significantly different. When using only the models in which the manually measured annulus and sinus both fell in the range of 24.2 – 28.2 mm and 29.2 – 33.2 mm respectively, it was found that sinus diameter measurements were not significantly different between the warped and manual measurement methods (table 11). Percent difference shows that the sinus was warped more accurately than the annulus.

Table 11 - Comparison of manual and HDW derived measurements

	Annulus				Sinus			
	warped mean	**manual mean**	**Paired t-test**	**% diff**	**warped mean**	**manual mean**	**Paired t-test**	**% diff**
All (N=95)	28.2 ±0.6	24.4 ±2.7	P<0.0001	16%	33.3 ±1.4	33.6 ±4.6	P=0.4598*	0.8%
Annulus matched (24.2 - 28.2 mm, N=42)	28.4 ±0.6	25.8 ±1.1	P<0.0001	10%	33.9 ±1.2	35.6 ±3.5	P=0.0018	4.7%
Sinus matched (29.2 - 33.2 mm, N=29)	28.0 ±0.4	23.3 ±1.7	P<0.0001	20%	32.9 ±0.8	31.3 ±0.9	P<0.0001	5.1%
Annulus & sinus matched (N=9)	27.9 ±0.4	25.2 ±1.0	P<0.0001	11%	32.9 ±0.9	31.7 ±0.7	P=0.0317	3.8%

* indicates results are **not** significantly different

High dimensional warping proved better when there was little difference between the images being warped. Some models warped very well (figure 26a), and some models warped poorly, even when they were of similar size (figure 26d). Initial registration appeared to be important to warping success.

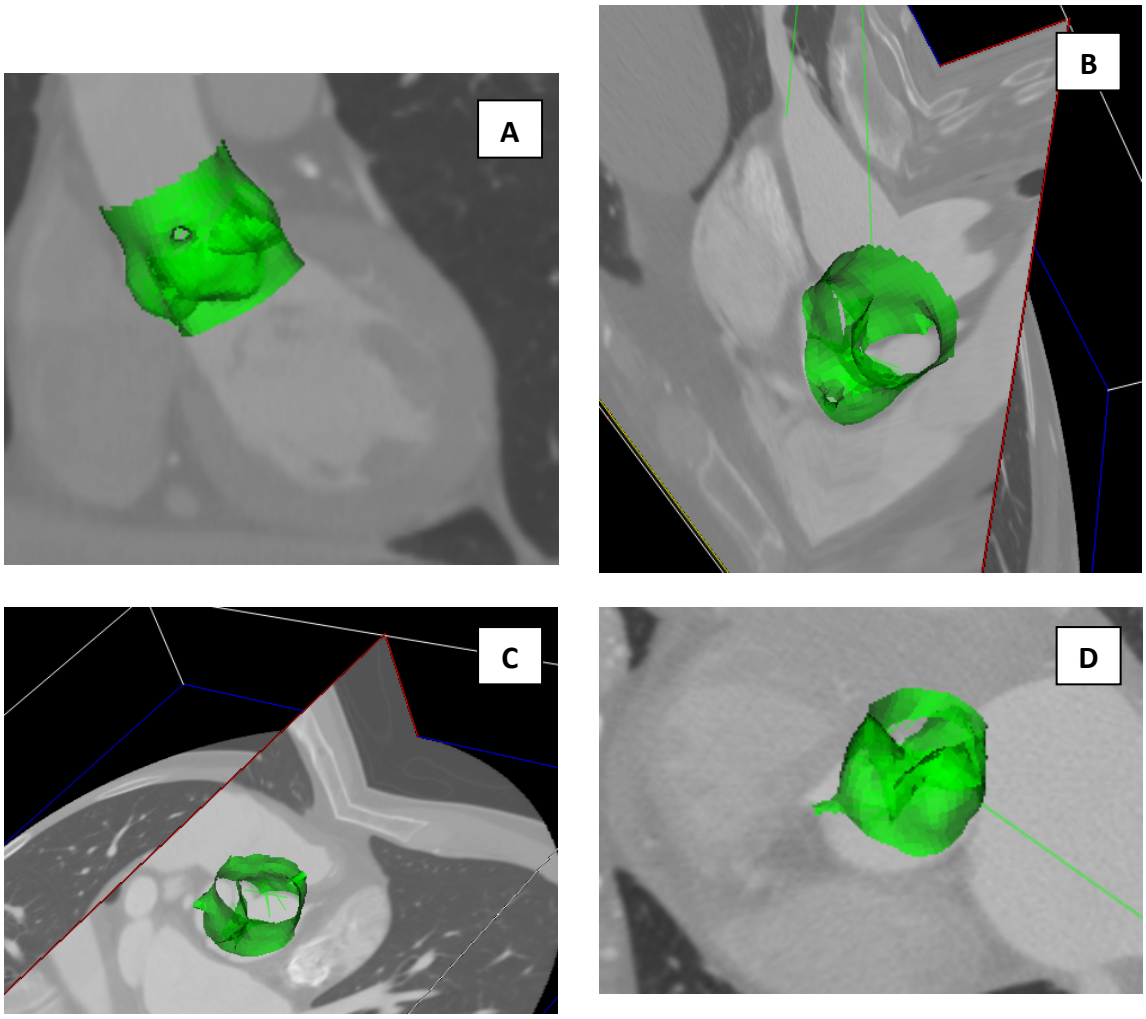

Figure 26 - Model fitting after warping. A) original manually picked model B) model with good fit <1 mm difference C) model with acceptable fit 1-2 mm D) model with poor fit >5 mm

3.7 - Point Distribution Model Creation

The PDMs created from 95 warped models, 95 scaled models, 42 annulus matched models, 29 sinus matched models, and 9 annulus & sinus matched models contained 64, 1, 33, 24, and 8 significant mode(s) of variation respectively. Each model contained 1446 landmarks, creating a covariance matrix of 4338 x 4338 elements. Running on an Intel Core 2 Duo 3.16 GHz CPU with 4GB of RAM, it took MATLAB approximately 9 minutes to calculate the eigenvectors and eigenvalues from the covariance matrix of each of the PDMs.

Images with primary mode of variation between -5 and +5 standard deviations of the mean are shown for each PDM in figure 27.

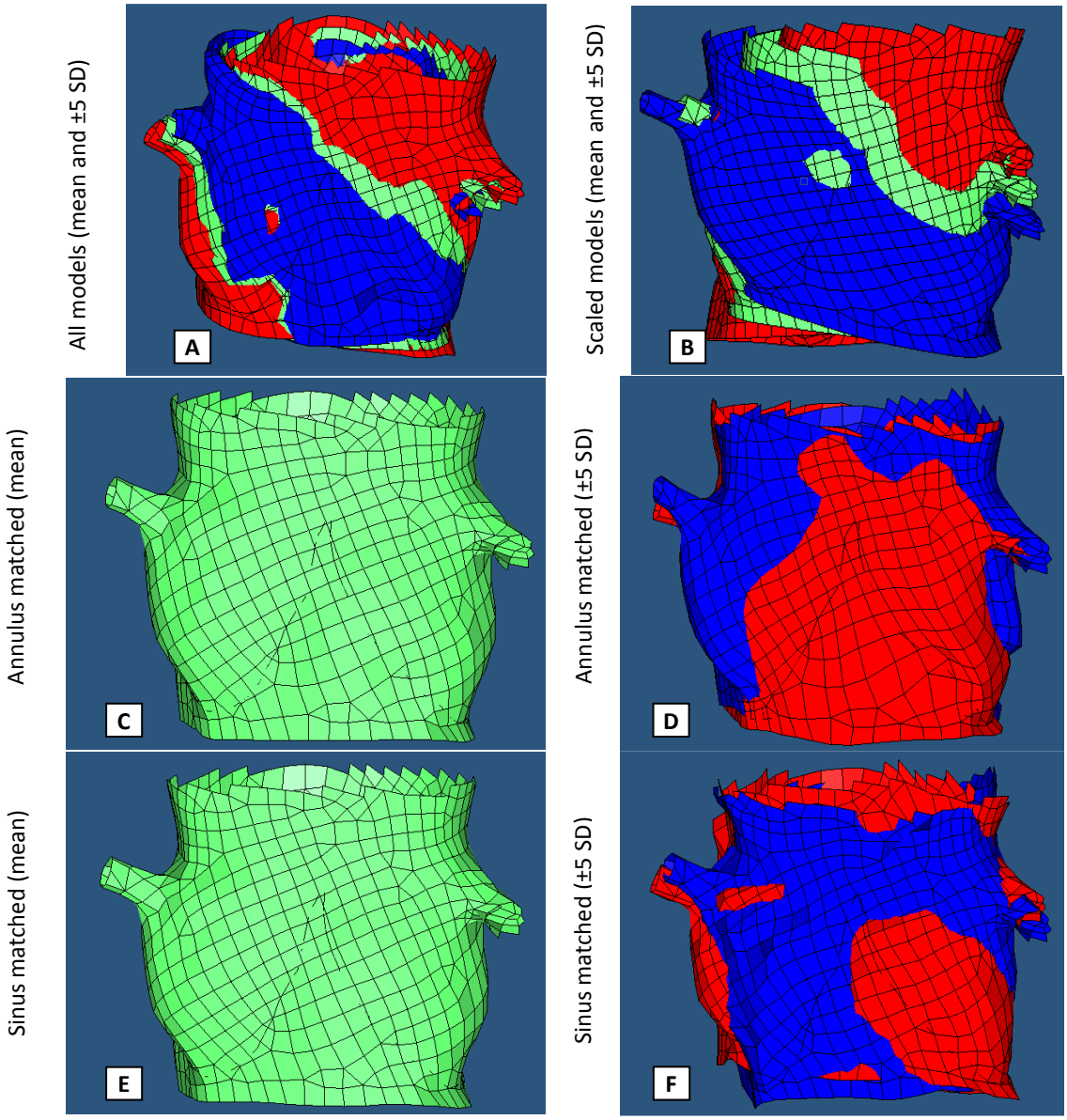

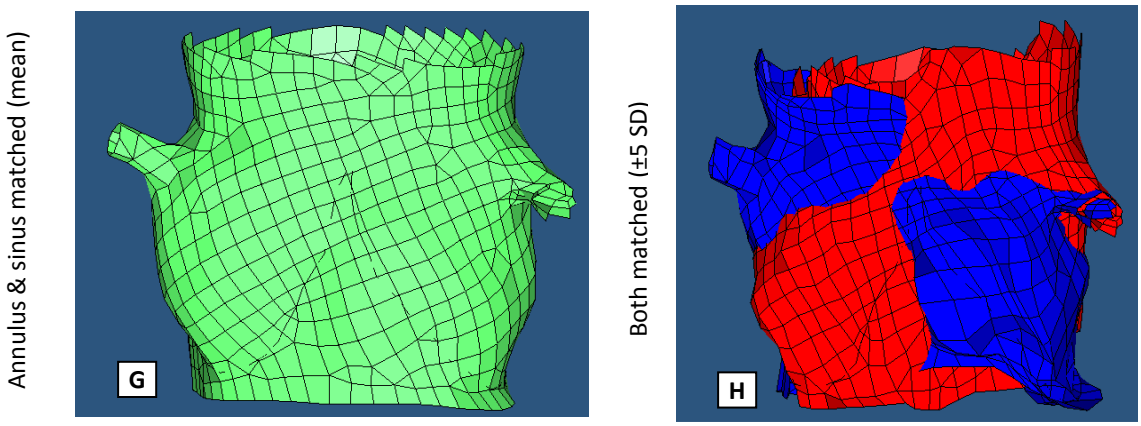

Figure 27 – Mean models and models varied by +/-5 standard deviations for the first mode of variation. i.e. the b value for the most significant eigenvector is varied
[ALL models: red +5 S.D., green mean model, blue -5 S.D.]

4 - Discussion

The Tissue Mechanics Laboratory at UConn had limited access to cardiac CT data prior to the start of this study. Most data was in the form of 2D screenshots obtained from radiology workstations, which was not ideal for 3D experimentation. While not groundbreaking, much of the contributions from this study will go toward establishing CT imaging as a basis for evaluating the mechanics of valve replacements.

4.1 - Clinical Assessment

The first step to understanding the imaging of the valves was to start at the beginning, and to understand how the valve is currently measured in clinical practice. Manual 2D measurement results from 95 patients confirm that our dataset is consistent with previous assessment studies of the aortic valve.

We found a mean annulus diameter of 24.4 mm, which is very similar to annulus diameters of 24.9 mm, 24.6 mm, and 24.1 mm reported by Tops et al, Messika-Zeitoun et al, and Schultz et al respectively [17, 23, 24]. A large variability in annulus diameter was found in our results, from 17.9 mm to 31.6 mm. This variability was not dependent on age, but was dependent on gender, with females having significantly smaller diameters. Large variability

(8.5 to 28.5 mm) was also found in the distance from the annulus to the closest ostium of the coronary arteries, which is similar to the range of 7.1 to 22.7 mm found in a previous study [23]. A common TAV manufactured by Edwards Scientific, with a height of 14.5mm and placed at a 50/50% orientation about the annulus, would not occlude the ostia of any patients in our sample. The ostium of the LCA was lower than the RCA in 75% of patients, so the LCA would have a higher chance of occlusion than the RCA. Of note, one patient excluded because of poor image quality did have the left coronary ostium below the leaflet coaptation.

Diameter at the LCA was larger than diameter at the RCA, which is reasonable considering the LCA is closer to the SOV. Our measurements showed the expected bulb shape of the aortic valve body, with the sinus having the largest diameter, and since the LCA was on average closer to the sinus than the aorta it is reasonable that diameter at LCA would be larger.

Consistent with previous studies, the aortic annulus was shown to have an elliptical shape [17, 23, 24, 57], and the eccentricity decreased as the diameter measurement was more proximal to the aorta. Few measures of central coaptation length exist in the literature, however previous studies showed that coaptation length was between 0.17 and 0.2 times the aorta diameter in cadaver hearts [60, 61]. Using these ratios, we would expect coaptation lengths of 5.0 – 5.9 mm based on our measured aorta diameter of 29.6 mm. This ratio is not consistent with our measured coaptation length of 2.5 mm *in vivo*.

Of particular interest were differences in measurements between gender and age groups. No differences existed between any height or diameter measurements between age groups, but significant differences were found between genders. Males had consistently larger diameter measurements than females, however only the annulus to aorta distance

was significantly different. P-values in Table 4 showed that a significant difference between genders appeared to be correlated with the magnitude of the measurements, where the significance level decreased as the mean measurements became smaller. This correlation may be an effect of the 1.25mm slice resolution of the images, in that a higher slice resolution may show significant differences between genders.

4.1.1 – Oblique versus sagittal/coronal slice planes

We experimented with the standard measurement method of creating an oblique slice plane across the short axis of the valve and taking measurements in that plane. Tops et al, in their 2008 study, still used the sagittal and coronal views to perform their assessments, which is most likely why their measurements are much different than those obtained from other studies including ours. Indeed our results showed a difference between major/minor axis measurements in the oblique plane to be 7 mm, while there was only a difference of 3.4mm when measuring the sagittal/coronal planes. Clearly the more comprehensive measurement method is to use oblique planes.

4.2 - 2D Automatic Measurement

Measurements obtained from the automatic segmentation algorithm were consistent with those found with the manual method, with a measurement difference rate below 5%. An automatic algorithm is advantageous to a manual method when measuring large image batches, and also allows quick measurements including perimeter and area. More importantly, an automatic algorithm is objective and not subject to human error. It can offer a second rating and augment human measurements. While an automatic algorithm is completely objective, its results do not always agree with manual measurements. While more precise, the measurements from the automatic algorithm were on average 1.2 mm smaller than manual measurements, which is most likely the result of CT image distortion by the point spread function (PSF) of the scanner. A PSF makes the edges of the structures

to appear blurred and as a result, the manual raters perceive the structures slightly larger than they actually are. An objective observation of annulus diameter is important when considering the implications of PPM in a TAVI.

4.2.1 – Perimeter versus direct measurement

For the 2D automatic method, the direct diameter measurements were compared to the diameters calculated using perimeters (Table 7). Paired t-tests (Table 9) showed that all diameters calculated from perimeter measurements were significantly larger ($p < 0.001$) than those by direct measurement, which implied that direct 2D diameter measurements might underestimate the real diameter of the aortic annulus. In addition, it should be noted that the perimeter of the annulus, P, can be approximated by

$P \cong \pi\left[3(a+b) - \sqrt{(3a+b)(a+3b)}\right]$ with a denoted as the major/coronal semi-axis length and b as the minor/sagittal semi-axis length of the annulus obtained from 2D cross-sectional views [62]. The calculated P was significantly smaller ($p < 0.001$) than the actual perimeter measurements obtained from the 2D automatic segmentation. This discrepancy suggested that direct diameter measurement in major/minor axes or coronal/sagittal views might not be sufficient to describe the actual perimeter of the aortic annulus. For TAVI prosthesis sizing, the actual perimeter of the aortic annulus should be used.

4.3 – 3D Manual Measurement

Similar to the way measurements obtained from oblique slice planes are more accurate than those obtained from orthogonal slice planes, 3D measurements may be more accurate than 2D measurements. Diameters calculated from perimeter measurements by 2D automatic and 3D manual methods were compared using paired t-tests. It was observed in Table 6 that there was no significant difference in diameters of the aortic annulus and AA between the two methods. Conversely, statistically significant difference ($p < 0.001$) in the SOV diameter was found between the two methods. The reason for this discrepancy could

be that the 2D and 3D perimeter measurements were taken on different cross-sectional planes. It is challenging to locate the accurate position of the cross-sectional plane from 2D views in order to precisely characterize the hemispherical shape and to find the largest diameter of the SOV; the selection of the cutting plane could be optimized by reviewing its position on 3D aortic root representations. By contrast, because of the less complex shapes of the aortic annulus and AA, their diameters calculated from perimeter measurements were affected by the selection of the cross-sectional plane to a lesser extent.

In addition, the LCA and RCA ostium heights obtained by 3D manual measurement (Table 8) were lower than the values by 2D manual measurement. This difference could be due to the fact that, compared to 2D manual measurement where a single 2D long-axis plane was utilized to measure the distance between coronary ostia and aortic annulus, it was easier to detect the inferior boundary of the coronary ostia from the 3D reconstructed aortic valve models. Therefore, more accurate measurements of the coronary ostia heights might be obtained by 3D method.

4.3 – HDW & PDM Algorithm Implementation

Implementation of effective image segmentation and feature identification algorithms appears to follow closely behind the increases in computational power available at the time. Articles about the theory of an image analysis algorithm are not as impressive as actually seeing results, and we are fortunate to currently see many algorithms such as quick facial recognition implemented in the past decade. These developments would not have been possible without the increase in computational speed of CPUs.

As an example, it is stated that the HDW algorithm took more than 15 hours to warp two 256x256x108 voxel brain images on a powerful workstation [54]. What took 15 hours ten years ago would take less than an hour today on standard hardware. These increases

make it possible to test complex algorithms in a reasonable period of time. Warping 95 80x80x80 voxel volumes to a single template took just over two hours on a Core 2 Duo 3.16GHz processor, which by the previous example would have taken more than 30 hours. When tweaking the HDW parameters in this study to find the best warping, it was possible to rerun the warping every two hours. This may have been impractical a decade ago.

4.4 - High Dimensional Warping and Landmark Propagation

With increased computational power available, we were able to test a novel approach to automatic landmark propagation. The goal of using HDW was to reduce the amount of time necessary to manually landmark dozens of training images. In 2D, it is not unreasonable to landmark 30 training images, each with 50 points. Landmarks from the previously marked image can simply be overlaid on the next image and the points moved about into the correct locations. In 3D this becomes extremely difficult because the number of landmarks is increased by the number of slices, and the ability to follow landmarks between slices is difficult.

Our methods of automatic landmarking for use with shape models were similar to those by van Assen et al, where a series of images were registered together and a standard set of landmarks was back-propagated to each model by inverting the registration [34]. Our approach went a step further and attempted to warp the images to a template and then back-propagate the landmarks which were established on the template.

Results from the HDW indicate that the template and target images must be very close in shape and size before attempting the warping. In our results, the models created from warping were not significantly different from manually measured dimensions if both the annulus and sinus diameters were already similar. If either the sinus or annulus was

very different to begin with, then the warping was not always accurate. When creating a training model

5 - Conclusion

The methods explored in this study were effective in creating models of the aortic valve with inherent variability. Results from our three measuring methods confirm their efficacy when compared against previous studies. Two dimension automatic measurement appears to be just as effective as manual measurement, but has the added benefit of being completely objective. Three dimensional measurement goes a step further than traditional measurement when assessing valve dimensions because it takes into account the variability of anatomy between slices.

High dimensional warping may be an effective method for automatic landmarking prior to creation of PDMs for use in AAMs. Though the method depends heavily on the performance of the warping, the principle is simple and effective. When used with similar sized structures, the warping can be quite accurate.

As a first venture into 3D image analysis by a mechanics laboratory, the work completed in this study should pave the way for future imaging work.

6 - Future Work

Using high dimensional warping to propagate landmarks was just the first step of applying active appearance models to target searching in patient images. It turns out the initial point distribution model is not critical to the success of the searching functions. The training of the AAM can be continuous: adding in successful fits and discarding unsuccessful fits. What remains after extensive training in this way is a PDM that represents the data better than a PDM created from automatically selected landmarks.

The primary goal for future work is to continue the implementation of 3D AAM searching now that a method for training has been established. Using the 1446 landmark model from this study may not be ideal, however, because of the small distances between landmarks. Successful fitting algorithms like those by Ionasec et al do not use very large PDMs, but instead interpolate points between major landmarks using splines [36, 43, 44]. This method is actually preferable to using a very detailed model because the more detailed a model, the less deformable it becomes.

To allow more deformation from warping and therefore add more sets of data to training, alternate methods of warping may be examined for effectiveness. HDW was one of the early 3D anatomic deformation methods, with little ability to control deformation extent. HDW works on principle of finding a deformation field and its inverse that best warps two images to each other. An alternate method called DARTEL (diffeomorphic anatomical registration through exponentiated lie algebra uses a slightly different method to achieve warping [63]. Instead of warping an entire image to another image, the DARTEL method first segments images into different tissue classes. These tissue classes are then registered and templates created based on the probability of a particular class occupying a particular voxel. Templates are applied to target images and warping is performed based on each segmented tissue class, not on all image intensities. This in theory should produce better warping because warps are only performed on regions of similar intensity. While ideal for 3D AAMs, other segmentation methods appear to bypass the intensive training necessary. Algorithms developed by Ionasec et al, which use sparse models based on splines instead of detailed landmark data, are extremely appealing because of their simplicity. Future work on patient specific model extraction may include parts of all of the methods examined in this paper.

Appendix A - Abbreviations

AAM – Active appearance model
ASM – Active shape model
AS – Aortic stenosis
AV – Aortic valve
FEM – Finite element model
HDW – High dimensional warping
LCA – Left coronary artery
LCL – Left coronary leaflet
MDCT – Multi-detector row computed tomography
NCL – Non-coronary leaflet
PAVR – Percutaneous aortic valve replacement
PCA – Principle components analysis
PDM – Point distribution model
RCA – Right coronary artery
RCL – Right coronary leaflet
SOV – Sinus of Valsalva
TAVI – Transcatheter aortic valve implantation

Appendix B – MATLAB sample code

B.1 – Landmark propagation

```
% read in template point file
points = dlmread(templatePointsFilename, '\t');
% get list of images to be unwarped
filelist = dir(filePattern);

for i=1:size(filelist)
    fname = filelist(i).name;
    warpedImage = ['y_' fname]; % the warped target image

    % read in the warped image data
    yvol = nifti(warpedImage);

    % create temp volumes for the trilinear interpolation
    volx = yvol.dat(:,:,:,:,1);
    voly = yvol.dat(:,:,:,:,2);
    volz = yvol.dat(:,:,:,:,3);

    for j=1:size(points,1)
        x = points(j,1);
        y = points(j,2);
        z = points(j,3);

        % MATLAB likes arrays to start at 1, not 0
        if x < 1
            x = 1;
        end
        if y < 1
            y = 1;
        end
        if z < 1
            z = 1;
        end

        % using the quicker trilinear method
        mm(2) = trilinear(volx,x,y,z) + 1;
        mm(1) = trilinear(voly,x,y,z) + 1;
        mm(3) = trilinear(volz,x,y,z) + 1;

        newpoints(j,1) = mm(1);
        newpoints(j,2) = mm(2);
        newpoints(j,3) = mm(3);
    end
end
```

B.2 – Point Distribution Model Creation and Alteration

```
% populate filelist
% M = number of points
% N = number of models
% ____________________________________________________
pointInitial = dlmread(filelist{1}, '\t'); % [Mx3] points
alignedPoints(:,:,1) = pointInitial(:,:);
```

```
for i=2:size(filelist,2)
    % align model i to model 1
    pointCurrent = dlmread(filelist{i}, '\t');
    [D pointsAligned] = procrustes(pointInitial, pointCurrent);
    alignedPoints(:,:,i) = pointsAligned(:,:); %[Mx3xN]
end

MeanShape = mean(alignedPoints,3); % [Mx3]
% concatenate the mean x,y,z points into 1 row
MeanX = single(squeeze(MeanShape(:,1,:)));
MeanY = single(squeeze(MeanShape(:,2,:)));
MeanZ = single(squeeze(MeanShape(:,3,:)));
MeanXYZ = [MeanX;MeanY;MeanZ]; % [3Mx1]

x = single(squeeze(alignedPoints(:,1,:)));
y = single(squeeze(alignedPoints(:,2,:)));
z = single(squeeze(alignedPoints(:,3,:)));
% concatenate and transform the aligned points into 1 row for each
model
xyz = [x;y;z]'; % [Nx3M]

% calculate covariance, eigenvectors, eigenvalues
CovMatrix=cov(xyz);  % --> [3Mx3M]
[pc, latent, explained] = pcacov(CovMatrix);
% determine the eigenvectors that describe largest 98% of the variance
higher=find(cumsum(explained)>=0.98);
EigenVectors=pc(:,1:higher(1));
EigenValues=latent(1:higher(1));
```

Appendix C – Software

The work done in this study required several software programs, some commcerial, some open-source, and some custom written. Below is a listing of sources of software used in this study.

- **MIView** (Medical Image Viewer) *open source*: custom designed prior to this study. Converts from DICOM to Analyze, Nifti, and raster image formats. Displays 3D image volumes from different flavors of DICOM, Analyze, Nifti, and raster. De-identifies DICOM data. Available from (http://gbooksoft.com)
- **Mricro & Mricron** *open source*: Analyze and Nifti display programs. Used to display orthogonal views of 3D and 4D Nifti data. Mricron is designed primarily to read/display Nifti data, but Mricro has more functionality. Available from (http://www.cabiatl.com/mricro)
- **VTKPointPicker** *open source*: Displays DICOM volumes from which landmark points can be selected, distances measured, and Abaqus meshes displayed. Available from (https://sourceforge.net/projects/vtkpointpicker)
- **SPM** (Statistical Parametric Mapping) *open source*: Software package to analyze functional (fMRI) and structural (sMRI) brain data. Includes voxel based morphometry (VBM) and EEG analysis tools. The high dimensional warping toolbox was the primary use for this software. Available from (http://www.fil.ion.ucl.ac.uk/spm)
- **HyperMesh** *commercial*: Used to build and display FEM meshes. Available from (http:// www.AltairHyperWorks.com/HyperMesh)
- **Mimics** *commercial*: Used to segment DICOM volumes and generation of FEM meshes. Available from (http://www.materialise.com/mimics)

References

1. Martini, F. and W.C. Ober, *Fundamentals of anatomy & physiology*. 7th ed. 2006, San Francisco, CA: Pearson Benjamin Cummings. 1 v. (various pagings).
2. Thubrikar, M., *The Aortic Valve*. 1 ed. 1990, Boca Raton, FL: CRC Press. 221.
3. Anderson, R.H., *The surgical anatomy of the aortic root.* Multimedia Manual of Cardiothoracic Surgery, 2007. **002527**: p. 8.
4. Anderson, R.H., *Clinical anatomy of the aortic root.* Heart, 2000. **84**(6): p. 670-3.
5. Weinberg, E.J., F.J. Schoen, and M.R. Mofrad, *A computational model of aging and calcification in the aortic heart valve.* PLoS One, 2009. **4**(6): p. e5960.
6. William C Roberts, J.M.K., *Valvular Heart Disease*. Comptemporary Cardiology, ed. T.B. Andrew Wang. 2009: Humana Press.
7. Routledge, H.C., et al., *Percutaneous aortic valve replacement: new hope for inoperable and high-risk patients.* J Invasive Cardiol, 2007. **19**(11): p. 478-83.
8. Webb, J.G., et al., *A new transcatheter aortic valve and percutaneous valve delivery system.* J Am Coll Cardiol, 2009. **53**(20): p. 1855-8.
9. Leon, M.B., et al., *Transcatheter aortic-valve implantation for aortic stenosis in patients who cannot undergo surgery.* N Engl J Med, 2010. **363**(17): p. 1597-607.
10. Rodes-Cabau, J., et al., *Transcatheter aortic valve implantation for the treatment of severe symptomatic aortic stenosis in patients at very high or prohibitive surgical risk: acute and late outcomes of the multicenter Canadian experience.* J Am Coll Cardiol, 2010. **55**(11): p. 1080-90.
11. Ye, J., et al., *Transapical transcatheter aortic valve implantation: follow-up to 3 years.* J Thorac Cardiovasc Surg, 2010. **139**(5): p. 1107-13, 1113 e1.
12. Charles Yankah, Y.W., Roland Hetzer, *Aortic Root Surgery - The Biological Solution*. 2010, Berlin, Germany: Springer. 599.
13. Webb, J.G., et al., *Percutaneous aortic valve implantation retrograde from the femoral artery.* Circulation, 2006. **113**(6): p. 842-50.
14. Jilaihawi, H., et al., *Prosthesis-patient mismatch after transcatheter aortic valve implantation with the Medtronic-Corevalve bioprosthesis.* Eur Heart J, 2009.
15. Sun, W., K. Li, and E. Sirois, *Simulated elliptical bioprosthetic valve deformation: Implications for asymmetric transcatheter valve deployment.* J Biomech, 2010. **43**(16): p. 3085-90.
16. Rees, M.R., et al., *Demonstration of mitral and aortic valves by ultrafast computed tomography.* J Comput Tomogr, 1987. **11**(2): p. 190-2.
17. Messika-Zeitoun, D., et al., *Multimodal assessment of the aortic annulus diameter: implications for transcatheter aortic valve implantation.* J Am Coll Cardiol, 2010. **55**(3): p. 186-94.
18. Ryan, R., et al., *Cardiac valve disease: spectrum of findings on cardiac 64-MDCT.* AJR Am J Roentgenol, 2008. **190**(5): p. W294-303.
19. Vogel-Claussen, J., et al., *Cardiac valve assessment with MR imaging and 64-section multi-detector row CT.* Radiographics, 2006. **26**(6): p. 1769-84.
20. Pannu, H.K., et al., *Gated cardiac imaging of the aortic valve on 64-slice multidetector row computed tomography: preliminary observations.* J Comput Assist Tomogr, 2006. **30**(3): p. 443-6.
21. Manghat, N.E., et al., *Imaging the heart valves using ECG-gated 64-detector row cardiac CT.* Br J Radiol, 2008. **81**(964): p. 275-90.

22. Niizeki, T., et al., *Quadricuspid aortic valve illustrated by 64-slice multidetector computed tomography: Surgical treatment of a rare cause of severe aortic regurgitation.* Journal of Cardiology Cases, 2010. **2**(1): p. e8-e11.
23. Tops, L.F., et al., *Noninvasive evaluation of the aortic root with multislice computed tomography implications for transcatheter aortic valve replacement.* JACC Cardiovasc Imaging, 2008. **1**(3): p. 321-30.
24. Schultz, C.J., et al., *Three dimensional evaluation of the aortic annulus using multislice computer tomography: are manufacturer's guidelines for sizing for percutaneous aortic valve replacement helpful?* Eur Heart J, 2009.
25. Lorensen, W.E. and H.E. Cline, *Marching cubes: A high resolution 3D surface construction algorithm.* SIGGRAPH Comput. Graph., 1987. **21**(4): p. 163-169.
26. Kass, M., A. Witkin, and D. Teropolous, *Snakes: Active Contour Models.* International Journal of Computer Vision, 1987: p. 321-331.
27. Cootes, T.F., et al., *Active Shape Models - Their Training and Application.* Computer Vision and Image Understanding, 1995. **61**(1).
28. Cootes, T.F., C.J. Taylor, and A. Lanitis. *Active Shape Models: Evaluation of a Multi-Resolution Method for Improving Image Search*. in *British Machine Vision Conference*. 1994: BMVA Press.
29. Cootes, T.F., G.J. Edwards, and C.J. Taylor, *Active Appearance Models.* Proc. European Conference on Computer Vision, 1998. **2**: p. 484-498.
30. Xiao, J., et al., *Real-time combined 2D+3D Active Appearance Models.* Proceedings of the IEEE Conference on Computer Vision and Pattern Recognition, 2004.
31. Babalola, K.O., et al., *3D brain segmentation using active appearance models and local regressors.* Med Image Comput Comput Assist Interv Int Conf Med Image Comput Comput Assist Interv, 2008. **11**(Pt 1): p. 401-8.
32. Heimann, T. and H.P. Meinzer, *Statistical shape models for 3D medical image segmentation: a review.* Med Image Anal, 2009. **13**(4): p. 543-63.
33. Heimann, T., I. Wolf, and H.P. Meinzer, *Active shape models for a fully automated 3D segmentation of the liver--an evaluation on clinical data.* Med Image Comput Comput Assist Interv Int Conf Med Image Comput Comput Assist Interv, 2006. **9**(Pt 2): p. 41-8.
34. van Assen, H.C., et al., *SPASM: a 3D-ASM for segmentation of sparse and arbitrarily oriented cardiac MRI data.* Med Image Anal, 2006. **10**(2): p. 286-303.
35. Staib, L.H. and J.S. Duncan, *Model-based deformable surface finding for medical images.* IEEE Trans Med Imaging, 1996. **15**(5): p. 720-31.
36. Ionasec, R.I., et al., *Patient-specific modeling and quantification of the aortic and mitral valves from 4-D cardiac CT and TEE.* IEEE Trans Med Imaging, 2010. **29**(9): p. 1636-51.
37. Votta, E., et al., *3D Computational Models for the Simulation of Mitral Valve Annuloplasty*, in *Summer Bioengineering Conference*. 2003: Key Biscayne, Florida.
38. Jiang, H., G. Campbell, and F. Xi, *Measurement and reconstruction of the leaflet geometry for a pericardial artificial heart valve.* Med Eng Phys, 2005. **27**(2): p. 175-80.
39. Zhang, H., et al., *4D Cardiac MR Image Analysis: Left and Right Ventricular Morphology and Function.* IEEE Trans Med Imaging, 2009.
40. Frangi, A.F., et al., *Automatic construction of multiple-object three-dimensional statistical shape models: application to cardiac modeling.* IEEE Trans Med Imaging, 2002. **21**(9): p. 1151-66.
41. Zhu, Y. and X. Papademetris, *Segmentation of the Left Ventricle From Cardiac MR Images Using a Subject-Specific Dynamical Model.* IEEE Trans Med Imaging, 2009.

42. Andreopoulos, A. and J.K. Tsotsos, *Efficient and generalizable statistical models of shape and appearance for analysis of cardiac MRI.* Med Image Anal, 2008. **12**(3): p. 335-57.
43. Ionasec, R.I., et al., *Dynamic model-driven quantitative and visual evaluation of the aortic valve from 4D CT.* Med Image Comput Comput Assist Interv Int Conf Med Image Comput Comput Assist Interv, 2008. **11**(Pt 1): p. 686-94.
44. Grbic, S., et al., *Complete valvular heart apparatus model from 4D cardiac CT.* Med Image Comput Comput Assist Interv, 2010. **13**(Pt 1): p. 218-26.
45. Theodoridis, S. and K. Koutroumbas, *Pattern recognition*. 2nd ed. 2003, Amsterdam ; Boston: Academic Press. xiv, 689 p.
46. Stegmann, M.B. and R. Fisker, *On Properties of Active Shape Models*. 2000: Lyngby, Denmark.
47. Hamarneh, G., R. Abu-Gharbieh, and T. Gustavsson. *Active Shape Models - Part I: Modeling Shape and Gray Level Variations*. in *Swedish Symposium on Image Analysis*. 1998.
48. Abu-Gharbieh, R., G. Hamarneh, and T. Gustavsson. *Active Shape Models - Part II: Image Search and Classification*. in *Swedish Symposium on Image Analysis*. 1998.
49. wikipedia. *Procrustes Analysis*. 2008 [cited 2008 September 30]; Available from: http://en.wikipedia.org/wiki/Procrustes_analysis.
50. Cootes, T.F., et al., *Active Shape Models - Their Training and Application.* Computer Vision and Image Understanding, 1995. **61**(1): p. 38-59.
51. Bishop, C.M., *Pattern recognition and machine learning*. Information science and statistics. 2006, New York: Springer. xx, 738 p.
52. Ashburner, J., J.L. Andersson, and K.J. Friston, *High-dimensional image registration using symmetric priors.* Neuroimage, 1999. **9**(6 Pt 1): p. 619-28.
53. John Ashburner, K.F., *Statistical Parametric Mapping v8*, F.I. Laboratory, Editor. 2008, Wellcome Trust Centre for Neuroimaging: London, GB.
54. Frackowiak, R.S.J., *Human brain function*. 2nd ed. 2004, Amsterdam ; Boston: Elsevier Academic Press. xvi, 1144 p.
55. Zambal, S., *3D Active Appearance Models for Segmentation of Cardiac MRI Data*, in *Center for Virtual Reality and Visualization*. 2005, Technical University of Wien. p. 112.
56. Prince, J.L. and J.M. Links, *Medical imaging signals and systems*. 2006, Upper Saddle River, NJ: Pearson Prentice Hall.
57. Wood, D.A., et al., *Role of multislice computed tomography in transcatheter aortic valve replacement.* Am J Cardiol, 2009. **103**(9): p. 1295-301.
58. Stolzmann, P., et al., *Remodelling of the aortic root in severe tricuspid aortic stenosis: implications for transcatheter aortic valve implantation.* Eur Radiol, 2009. **19**(6): p. 1316-23.
59. Akhtar, M., et al., *Aortic root morphology in patients undergoing percutaneous aortic valve replacement: evidence of aortic root remodeling.* J Thorac Cardiovasc Surg, 2009. **137**(4): p. 950-6.
60. Swanson, W.M. and R.E. Clark, *Aortic valve leaflet motion during systole. Numerical-graphical determination.* Circ Res, 1973. **32**(1): p. 42-8.
61. Swanson, M. and R.E. Clark, *Dimensions and geometric relationships of the human aortic valve as a function of pressure.* Circ Res, 1974. **35**(6): p. 871-82.
62. Ramanujan, S., *Modular Equations and Approximations to Pi.* Quarterly Journal of Pure Applied Mathematics, 1913-1914. **45**: p. 350-372.
63. Ashburner, J., *A fast diffeomorphic image registration algorithm.* Neuroimage, 2007. **38**(1): p. 95-113.